

# The Mass Accretion Rate of Clusters of Galaxies: CIRS and HeCS

M. Pizzardo<sup>1,2</sup>, S. Di Gioia<sup>3,4,5</sup>, A. Diaferio<sup>1,2</sup>, C. De Boni<sup>6</sup>, A. L. Serra<sup>1,2</sup>, M. J. Geller<sup>7</sup>, J. Sohn<sup>7</sup>, K. Rines<sup>8</sup>, and M. Baldi<sup>9,10,11</sup>

<sup>1</sup> Dipartimento di Fisica, Università di Torino, via P. Giuria 1, I-10125 Torino, Italy

<sup>2</sup> Istituto Nazionale di Fisica Nucleare (INFN), Sezione di Torino, via P. Giuria 1, I-10125 Torino, Italy

<sup>3</sup> Dipartimento di Fisica, Università di Trieste, via A. Valerio, 2, I-34127 Trieste, Italy

<sup>4</sup> Istituto Nazionale di Astrofisica (INAF), Sezione di Trieste, via G.B. Tiepolo 11, I-34143 Trieste, Italy

<sup>5</sup> Istituto Nazionale di Fisica Nucleare (INFN), Sezione di Trieste, via A. Valerio 2, I-34127 Trieste, Italy

<sup>6</sup> OmegaLambdaTec GmbH, Lichtenbergstraße 8, D-85748 Garching, Germany

<sup>7</sup> Smithsonian Astrophysical Observatory, 60 Garden Street, Cambridge, MA-02138, USA

<sup>8</sup> Department of Physics and Astronomy, Western Washington University, Bellingham, WA-98225, USA

<sup>9</sup> Dipartimento di Fisica e Astronomia, Alma Mater Studiorum Università di Bologna, via Gobetti 93/1, I-40129 Bologna, Italy

<sup>10</sup> Astrophysics and Space Science Observatory Bologna, via Gobetti 93/2, I-40129, Bologna, Italy

<sup>11</sup> Istituto Nazionale di Fisica Nucleare (INFN), Sezione di Bologna, viale Berti Pichat 6/2, I-40127, Bologna, Italy

Received date / Accepted date

## ABSTRACT

We use a new spherical accretion recipe tested on N-body simulations to measure the observed mass accretion rate (MAR) of 129 clusters in the CIRS and HeCS. The observed clusters cover the redshift range  $0.01 < z < 0.30$  and the mass range  $\sim 10^{14} - 10^{15} h^{-1} M_{\odot}$ . Based on three-dimensional mass profiles of simulated clusters reaching beyond the virial radius, our recipe returns MARs that agree with MARs based on merger trees. We adopt this recipe to estimate the MAR of real clusters based on measurement of the mass profile out to  $\sim 3R_{200}$ . We use the caustic method to measure the mass profiles to these large radii. We demonstrate the solidity of our estimates by applying the same approach to a set of mock redshift surveys of a sample of 2000 simulated clusters with median mass  $M_{200} = 10^{14} h^{-1} M_{\odot}$ , and a sample of 50 simulated clusters with median mass  $M_{200} = 10^{15} h^{-1} M_{\odot}$ : the median MARs based on the caustic mass profiles of the simulated clusters are unbiased and agree within 17% with the median MARs based on the real mass profile of the clusters. The MAR of the CIRS and HeCS clusters increases with the mass and the redshift of the accreting cluster, in excellent agreement with the growth of clusters in the  $\Lambda$ CDM model.

**Key words.** galaxies: clusters: general - galaxies: kinematics and dynamics - methods: numerical

## 1. Introduction

In the current Cold Dark Matter (CDM) model of the formation and evolution of cosmic structures, smaller dark matter halos hierarchically aggregate into larger and more massive halos. The accretion occurs through mergers with halos of comparable, *major* mergers, or lower, *minor* mergers, mass and with the capture of diffuse dark matter particles (e.g., Press & Schechter 1974; White & Rees 1978; Lacey & Cole 1993; Bower 1991; Sheth & Tormen 2002; Zhang et al. 2008; De Simone et al. 2011; Corasaniti & Aчитouv 2011; Aчитouv et al. 2014; Musso et al. 2018).

In principle, the mass accretion of dark matter halos is a valuable tool to test different models of structure formation. Specifically, the mass evolution  $M(z)$  of a dark matter halo, which describes its mass assembling history, or its time derivative, the mass accretion rate  $\dot{M}(z)$ , can be used to determine the halo formation redshift (Lacey & Cole 1993; van den Bosch 2002; Ragone-Figueroa et al. 2010; Giocoli et al. 2012). The rates are correlated with halo properties including concentration (Wechsler et al. 2002; Tasitsiomi et al. 2004; Zhao et al. 2009; Giocoli et al. 2012; Ludlow et al. 2013), shape (Kasun & Evrard 2005; Allgood et al. 2006; Bett et al. 2007; Ragone-Figueroa

et al. 2010), spin (Vitvitska et al. 2002; Bett et al. 2007), degree of internal relaxation (Power et al. 2011), and fraction of substructures (Gao et al. 2004; Van Den Bosch et al. 2005; Ludlow et al. 2013). The assembly of dark matter halos can trace the accretion rate of baryons from the cosmic web onto the dark matter halo (van den Bosch 2002; McBride et al. 2009; Fakhouri et al. 2010).

In theoretical studies, the estimates of the mass accretion history (MAH),  $M(z)$ , and the mass accretion rate (MAR),  $\dot{M}(z)$ , of a dark matter halo at the present time are usually tackled by tracing the merger tree of the halo, either with numerical simulations (e.g., Genel et al. 2008; Kuhlen et al. 2012; Baldi 2012) or with Monte Carlo methods (Lacey & Cole 1993; Kauffmann et al. 1993; Somerville & Kolatt 1999; Parkinson et al. 2007; Jiang & van den Bosch 2014). In hierarchical clustering scenarios, by going back in time, the dark matter halo separates into two or more halos: at each epoch, the growing halo, the descendant, has a main progenitor, namely the most massive halo, that merges with smaller halos and generates the descendant. By identifying the main progenitor of the halo at each epoch, we can trace the formation history, or MAH, of a simulated halo by tracing the main branch of its merger tree.

In this framework, numerous studies investigate the MAH in  $\Lambda$ CDM cosmologies. Analytical approximations can describe the MAH as a function of the final mass of the halo and other additional parameters. For example, McBride et al. (2009), Fakhouri et al. (2010), and Correa et al. (2015) adopt the relation  $M(z) = M_0(1+z)^\beta e^{-\gamma z}$  for the growth in mass with redshift  $z$ , whereas van den Bosch (2002) and van den Bosch et al. (2014) adopt  $M(z) = M_0 \exp \left\{ \ln(1/2) \left[ \frac{\ln(1+z)}{\ln(1+z_f)} \right]^\nu \right\}$ . In the latter case the formation redshift  $z_f$  and  $\nu$  are left as free parameters, whereas in the former expression  $\beta$  and  $\gamma$  are left either free or fixed by the linear power spectrum of matter (Correa et al. 2015). In both formulae  $M_0$  is the halo mass at redshift  $z = 0$ .

These studies point out that the MAH can be separated into two regimes. In the first regime, at early times, the mass accretion is relatively large and the growth is nearly exponential in redshift: here, major mergers are efficient and keep the system unrelaxed. In the second regime, at later times, the accretion slows down and the growth is governed by a power-law in redshift, thus enabling the halo to reach virial equilibrium. These studies also show that more massive halos, that form at relatively low redshifts, have larger MAR than less massive halos. This correlation is supported by (1) the correlation between the age and the concentration and (2) the anti-correlation between the mass and the concentration of dark matter halos (Zhao et al. 2009). In other words, old, low-mass and highly concentrated dark matter halos should have lower MAR than young, high-mass and less concentrated halos.

The MAH can be a probe of the cosmological parameters. Hurier (2019) uses the thermal Sunyaev-Zel'dovich (SZ) effect, as proxy for the mass of the clusters from the second Planck SZ catalogue (Ade et al. 2016), and the fit by Correa et al. (2015) to the MAH of dark matter halos in simulations, to derive values for the power spectrum normalization  $\sigma_8$ , the cosmic mass density  $\Omega_m$ , and the Hubble parameter  $H_0$ ,  $\sigma_8(\Omega_m/0.3)^{-0.3}(H_0/70)^{-0.2} = 0.75 \pm 0.06$ , in rough agreement with other analyses of galaxy cluster samples and of the power spectrum of the Cosmic Microwave Background (de Haan et al. 2016; Planck Collaboration et al. 2018; Zubeldia & Challinor 2019).

The investigation of the MAH and the MAR is also connected to the splashback radius, the radius within which the material recently accreted by the halo splashes back. This radius is larger than the radii  $R_{200}$  or  $R_{\text{vir}}$  usually adopted to quantify the halo size, and is close to  $\sim 2R_{200}$ , on average (More et al. 2015). In their simulations, Diemer & Kravtsov (2014) find that the steepness of the slope of the halo mass profile at large radii increases with increasing MAR. Moreover, the cluster-centric radius of this change of slope decreases with increasing MAR. Adhikari et al. (2014) associate the location of this feature with the splashback radius.

A change of slope consistent with the expectations from the simulations is indeed present in the profile of the surface number density of galaxies from the Dark Energy Survey (DES) cross-correlated with the SZ clusters from the South Pole Telescope (SPT) and the Atacama Cosmology Telescope (ACT) (Shin et al. 2019), and in the deprojected cross-correlation of the SZ clusters from the Planck Survey with galaxies detected photometrically in the PanSTARRS survey (Zürcher & More 2019). Similarly, the splashback radius is detected in the inferred dark matter density profiles of the redMaPPer clusters (More et al. 2016), and in clusters from either the Sloan Digital Sky Survey (SDSS) (Baxter et al. 2017) or DES (Chang et al. 2018).

Although interlopers along the line of sight affect the inference of this feature both from optically selected clusters (Busch

& White 2017; Shin et al. 2019; Sunayama & More 2019) and from weak lensing analyses of X-ray selected clusters (Umetsu & Diemer 2017; Contigiani et al. 2019), dense galaxy redshift surveys (Geller et al. 2011; Serra & Diaferio 2013; Sohn et al. 2018; Rines et al. 2018) and upcoming lensing surveys might potentially overcome this contamination and constrain the relation between the splashback radius and the accretion rate (Xhakaj et al. 2019).

All these studies highlight the relevance of an observational estimate of the MAR of galaxy clusters. Unfortunately, only a handful of direct measurements have been attempted so far. In fact, we observe a real cluster at a given time and we cannot clearly identify its merger tree to quantify the MAR, as one usually does when  $N$ -body simulations are available. A viable approach that has been pursued with real clusters is to identify galaxy groups that surround the cluster and appear to fall onto it (e.g. Rines et al. 2001); unfortunately, the estimate of their masses does not provide an estimate of the MAR, but only a lower limit (e.g. Lemze et al. 2013; Haines et al. 2018).

More importantly, the cluster outer region needs to be properly chosen. For example, Lemze et al. (2013) investigate the region slightly beyond  $R_{200}$  in X-ray and the optical bands, whereas Tchernin et al. (2016) detect infalling gas clumps of A2142 in X-ray and SZ out to  $\sim 1.3R_{200}$ . Similarly, Haines et al. (2018) identify the infalling groups in the range  $(0.28; 1.35)R_{200}$ . According to studies of the splashback radius, these radii may be too small to return a full estimate of the MAR: in fact, we expect that these regions contain matter with rather different dynamical histories: matter that is falling onto the cluster for the first time, matter that is splashing outwards and matter that is falling back again.

To avoid this complex dynamical structure and return a proper estimate of the MAR, we thus have to consider a region which is further out, namely beyond the splash-back radius  $\sim 2R_{200}$ . We expect that this region contains matter that will fall onto the cluster in the near future rather than matter that is already trapped in the gravitational potential well of the cluster (De Boni et al. 2016; Haines et al. 2018).

In this paper we pursue this idea, originally suggested by De Boni et al. (2016). We estimate the MAR from the amount of mass in the cluster outer region beyond  $\sim 2R_{200}$ . Unfortunately, compared to the cluster central region, the cluster outskirts are a large and low-density region, where the system is not dynamically relaxed. The methods used to estimate the mass cannot rely on the hypothesis of virial equilibrium. The caustic method and weak gravitational lensing are two complementary methods that do not rely on this hypothesis (Geller et al. 2013) and are thus appropriate to estimate the amount of mass in these outer regions.

Here, we present the first estimation of the MAR of real clusters based on the spherical accretion model developed by De Boni et al. (2016). To estimate the cluster mass profiles in their outer region we use the caustic technique (Diaferio & Geller 1997; Diaferio 1999). The caustic technique is known to return an unbiased mass estimates with a relative uncertainty of 50%, or better, in the regions where the accretion takes place (Serra et al. 2011). Unlike methods based on weak gravitational lensing where the signal is stronger at intermediate redshift and rapidly drops at low and high redshift (Hoekstra 2003; Hoekstra et al. 2011), the caustic technique can be applied to clusters at any redshift, provided that the number of spectroscopic redshifts is large enough to sample the velocity field properly.

In Section 2, we briefly summarize the spherical infall method introduced in De Boni et al. (2016). In Section 3, we

use  $N$ -body simulations to test our method of estimating the MAR. Section 4 describes the CIRS and HeCS catalogues of real clusters that span the redshift range  $0 - 0.3$  and the mass range  $\sim 10^{14} - 10^{15} h^{-1} M_{\odot}$ . In Section 5, we illustrate and discuss the estimates of the MAR of individual clusters and the mean MAR of the cluster samples as a function of mass and redshift. We discuss our results in Section 6 and we conclude in Section 7. We adopt  $H_0 = 100 h \text{ km s}^{-1} \text{ Mpc}^{-1}$  throughout.

## 2. The spherical accretion recipe

In this section, we briefly review the model proposed in De Boni et al. (2016) to evaluate the MAR of clusters from spectroscopic redshift surveys.

De Boni et al. (2016) estimate the MAR from the merger trees of dark matter halos, of mass  $\sim 10^{14} h^{-1} M_{\odot}$ , extracted from  $N$ -body simulations. They find that, in the redshift range  $z = [0, 2]$ , a spherical accretion recipe returns an unbiased MAR within  $\sim 20\%$  of the average MAR from the merger trees. For the more massive halos of mass  $\sim 10^{15} h^{-1} M_{\odot}$ , although the statistics of De Boni et al. (2016) are rather poor and the MAR estimated with the spherical accretion recipe is  $\sim 10 - 40\%$  biased low, the recipe still returns a MAR within the  $1-\sigma$  spread of the MAR derived from the merger trees. In the spherical accretion recipe, the MAR is estimated by assuming that the mass within a spherical shell of proper thickness, centered on the cluster, will fully accrete onto the cluster within a given time interval  $t_{\text{inf}}$ . We assume that the massive shell falls onto the cluster with constant acceleration and a given initial proper velocity  $v_i$ . By solving the equation of motion, we end up with an equation whose unknown is the thickness  $\delta_s R_i$  of the shell, where  $R_i$  is the inner radius of the shell:

$$t_{\text{inf}}^2 G M(< R_i) - t_{\text{inf}} 2 R_i^2 (1 + \delta_s/2)^2 v_i - R_i^3 \delta_s (1 + \delta_s/2)^2 = 0, \quad (1)$$

where  $M(< R_i)$  is the mass of the cluster within the radius  $R_i$  and  $G$  is the gravitational constant.

We assume the inner radius of the shell is  $R_i = 2R_{200}$ , with  $R_{200}$  the radius within which the average density is 200 times the critical density of the Universe at the appropriate redshift. As anticipated in the Introduction, this radius  $R_i$  is close to the average splashback radius of massive halos of cluster size at redshift  $z < 2$  found in  $N$ -body simulations (More et al. 2015). This radius also approximates the inner radius of the region containing the mass that will fall onto clusters in the near future. In addition, close to  $R_i$ , the absolute value of the infall radial velocity generally reaches its maximum (Sect. 3.3) and the recipe thus includes the largest contribution to the MAR. The solution of Equation (1) yields the shell thickness  $\delta_s R_i$  and the mass of the shell  $M_{\text{shell}}$ , if the mass profile of the cluster at radii larger than  $2R_{200}$  is known.

The MAR is thus simply estimated as

$$\text{MAR} = \frac{dM}{dt} \equiv \frac{M_{\text{shell}}}{t_{\text{inf}}}. \quad (2)$$

This recipe still requires the values of  $t_{\text{inf}}$  and  $v_i$ , not currently measurable in real clusters.

For  $t_{\text{inf}}$  and  $v_i$  we resort to  $N$ -body simulations of dark matter halos of cluster size, assuming that these systems resemble real clusters. Clearly, these values can differ widely from halo to halo. To apply Equation (2) properly, we adopt an average value for both  $t_{\text{inf}}$  and  $v_i$  for samples of dark matter halos within proper mass and redshift bins. If the ranges covered by these bins are

sufficiently small, as we detail below, this approach can provide the MAR of a real cluster if its mass profile is known.

We measure the mass profile of real clusters to radii larger than  $R_{200}$  with the caustic technique. This technique uses redshift data alone and does not require the assumption of dynamical equilibrium; however, it assumes spherical symmetry and deviations from this symmetry are responsible for most of the uncertainty in the mass profile and, consequently, in the MAR.

## 3. Testing the mass accretion recipe on mock redshift surveys of clusters

Before applying the MAR recipe to real clusters, we need to evaluate the reliability of our MAR estimate and its possible systematic errors. Here, we test the recipe on mock redshift surveys of clusters extracted from an  $N$ -body simulation of a  $\Lambda$ CDM model. We also use this simulation to provide the proper values of  $t_{\text{inf}}$  and  $v_i$  for clusters in different bins of mass and redshift.

In Sects. 3.1 and 3.2 we describe the  $N$ -body simulation and the construction of the mock redshift surveys, respectively. In Sect. 3.3 we discuss the radial velocity profiles of the clusters in the simulation, and in Sect. 3.4 we illustrate how our estimate of the MAR from the redshift surveys compares with the MAR estimated with the full three-dimensional information.

### 3.1. CoDECS simulations

For our tests, similar to De Boni et al. (2016), we rely on the L-CoDECS simulations (Baldi 2012). L-CoDECS is a set of  $N$ -body numerical simulations of a  $\Lambda$ CDM cosmology and other quintessence models. Here we use only the  $\Lambda$ CDM run.

The simulations are normalized at the Cosmic Microwave Background epoch with cosmological parameters according to the WMAP7 analysis (Komatsu et al. 2011): cosmological dark matter density  $\Omega_{m0} = 0.226$ , cosmological constant  $\Omega_{\Lambda0} = 0.729$ , baryonic mass density  $\Omega_{b0} = 0.0451$ , Hubble constant  $H_0 = 70.3 \text{ km s}^{-1} \text{ Mpc}^{-1}$ , power spectrum normalization  $\sigma_8 = 0.809$ , and power spectrum index  $n_s = 0.966$ . The box size is  $1 h^{-1} \text{ Gpc}$  on a side in comoving coordinates, and the simulation contains  $1024^3$  dark matter particles with mass  $m_{\text{DM}} = 5.84 \times 10^{10} h^{-1} M_{\odot}$  and the same number of baryonic particles with mass  $m_b = 1.17 \times 10^{10} h^{-1} M_{\odot}$ . Baryons are included only to check fifth-force effects in the quintessence cosmologies, but no hydrodynamics is included in the simulation. The  $\Lambda$ CDM run is a standard collisionless  $N$ -body simulation.

Groups and clusters in the simulations are identified with a friends-of-friends algorithm with linking length  $\lambda = 0.2\bar{d}$ , where  $\bar{d}$  is the mean interparticle separation. The algorithm is only run over the dark matter particles. Each baryonic particle is associated with the closest dark matter particle at the end of the procedure.

We consider only the clusters in two different mass bins with median mass, within  $R_{200}$  at  $z = 0$ :  $M_{200} \simeq 10^{14} h^{-1} M_{\odot}$  and  $M_{200} \simeq 10^{15} h^{-1} M_{\odot}$ . The two samples contain  $N = 2000$  and  $N = 50$  clusters, respectively. We identify the main progenitors of these clusters and consider the samples of these progenitors at each redshift. We consider the outputs of the simulation at six different redshifts:  $z = 0.0, 0.12, 0.19, 0.26, 0.35, 0.44$ . Table 1 shows the median and the amplitude of the two mass bins at different redshifts.

**Table 1.** THE TWO SAMPLES OF SIMULATED CLUSTERS\*

$z$	median $M_{200}$ [ $10^{14} h^{-1} M_{\odot}$ ]	68 <sup>th</sup> percentile range [ $10^{14} h^{-1} M_{\odot}$ ]
0.00	1.00	0.97-1.04
0.12	0.95	0.75-1.07
0.19	0.90	0.64-1.06
0.26	0.85	0.56-1.02
0.35	0.78	0.49-0.96
0.44	0.69	0.43-0.89
0.00	10.0	9.5-11.2
0.12	8.2	6.8-10.9
0.19	7.3	5.2-9.6
0.26	6.1	4.4-8.4
0.35	5.4	4.0-7.5
0.44	4.7	3.2-6.1

\*The upper (lower) part of the table is for the clusters in the low-mass (high-mass) bin.

### 3.2. Mock catalogues and mass profiles

The first ingredient of the MAR recipe is the three-dimensional mass profile of the cluster extending to large radii. We use the caustic method to estimate this profile in real clusters. With a sufficiently dense redshift survey of the outer regions of an individual cluster, the caustic mass profile deviates from the real three-dimensional mass profile by less than 10%, on average, in the radial range  $[0.6, 4]R_{200}$ , with a  $1\sigma$  relative uncertainty of  $\sim 50\%$  (Serra et al. 2011).

The uncertainty in the caustic mass profile is due mostly to the assumption of spherical symmetry and clearly propagates into our estimate of the MAR. To quantify how this uncertainty propagates, we apply our MAR recipe to synthetic observations of the simulated clusters. We assume that the dark matter halos we model in our  $N$ -body simulation are a realistic representation of galaxy clusters, and that their dark matter particles trace the same velocity field of the real galaxies. The latter assumption seems to be appropriate, because hydrodynamical  $N$ -body simulations indicate that the velocity bias between dark matter particles and galaxies is smaller than  $\sim 10\%$  (Diemand et al. 2004; Hellwing et al. 2016; Armitage et al. 2018).

To create the mock redshift survey of a simulated cluster, we extract a squared-basis truncated pyramid centered on the cluster, with the smaller basis closer to the observer; the pyramid axis is aligned along one of the three cartesian coordinates chosen as the line of sight and has height  $2b_L = 140 h^{-1}$  Mpc. The sizes  $r_{\min}$  and  $r_{\max}$  of the two bases are defined by the intercept theorem  $r_s : r_{\text{FOV}}/2 = (r_s \mp b_L) : r_{\min, \max}$ , where  $r_s$  is the comoving distance of the cluster centre from the observer and  $r_{\text{FOV}}$  is the size of the field of view. We can use the previous relation appropriate for Euclidean geometry, because here we consider the flat  $\Lambda$ CDM model.

Similarly to Serra et al. (2011), we take  $r_{\text{FOV}} = 12 h^{-1}$  Mpc. This value easily covers even the most massive clusters out to a few virial radii.

For each cluster we build three mock catalogues, one for each cartesian coordinate chosen as the line of sight. In general, the clusters are not spherically symmetric. Thus to improve the statistics, we can consider these three mock catalogues as independent clusters even though they are not completely independent systems.

Each selected volume contains a number  $N_{14} = 35^{+16}_{-10} \times 10^3$  and  $N_{15} = 62^{+22}_{-14} \times 10^3$  of dark matter particles for the low- and high-mass bin respectively; the ranges shown indicate the 10<sup>th</sup> – 90<sup>th</sup> percentile ranges. In the same field of view, the densest survey of a real cluster contains a few thousand galaxies (e.g., Hwang et al. 2014; Sohn et al. 2019a). Therefore, to identify each dark matter particle with an individual galaxy, we randomly sample a limited number of dark matter particles within the volume. According to Serra et al. (2011), the caustic method performs better when the velocity field of the cluster is sampled by  $\sim 200$  galaxies within  $3R_{200}$  from the cluster centre. We follow this approach and sample the dark matter particles until we reach  $N_{\text{sample}} = 200$  particles within  $r = 3R_{200}$ . This procedure yields a number  $N_{14}^{\text{red}} = 300^{+170}_{-90}$  and  $N_{15}^{\text{red}} = 610^{+290}_{-130}$  of particles within each mock redshift survey for the high- and the low-mass bin, respectively.

The observed redshift  $z$  of each particle is set by its cosmological redshift and its peculiar velocity  $\mathbf{v}_p = \mathbf{u}_p/(1+z_s)$  in the comoving frame of the simulation box:  $z_s$  is the redshift of the simulation snapshot, and  $\mathbf{u}_p$  is the comoving peculiar velocity provided by the  $N$ -body simulation.<sup>1</sup>

The comoving distance from the observer to the centre of the simulation box, which coincides with the cluster centre, is  $r_s = c/H_0 \int_0^{z_s} dz'/E(z')$ , where  $E(z) = H(z)/H_0 = [(\Omega_{m0} + \Omega_{b0})(1+z)^3 + \Omega_{\Lambda}]^{1/2}$  in the flat  $\Lambda$ CDM model. The particle position vector in the observer reference frame is thus  $\mathbf{r}_i = \mathbf{r}_s + \mathbf{r}_{c,i}$ , where  $\mathbf{r}_{c,i}$  is the comoving position vector of the particle in the reference frame of the simulation box. This sum of vectors is derived in the Euclidean geometry of the  $\Lambda$ CDM model of the simulation.

The cosmological redshift  $z_i$  of the particle satisfies the relation  $r_i = c/H_0 \int_0^{z_i} dz'/E(z')$ , and the observed component of the peculiar velocity is  $v_{\text{los},i} = \mathbf{v}_p \cdot \mathbf{r}_i/r_i$ , where  $\mathbf{v}_p$  is the peculiar velocity of the particle mentioned above. The redshift due to the peculiar velocity is  $z_{p,i} = v_{\text{los},i}/c$ , because  $v_{\text{los},i} \ll c$ . Combining  $z_{p,i}$  with  $z_i$  yields the observed redshift  $(1+z_{\text{obs},i}) = (1+z_i)(1+z_{p,i})$ ,

<sup>1</sup> As velocity variable, the code Gadget-II used for the CoDECS simulations actually uses and returns the quantity  $\mathbf{w} = a^{1/2}\mathbf{u}_p$  as a remedy to the divergence of the comoving peculiar velocity field at small scale factors  $a$ ; this strategy maximizes the computational efficiency of the integration of the equations of motion at early times (Springel et al. 2001).

namely

$$cz_{\text{obs}} = cz_i + v_{\text{los},i}(1 + z_i). \quad (3)$$

Standard geometrical transformations finally yield the celestial coordinates  $(\alpha, \delta)$  from the cartesian components of  $\mathbf{r}_i$ .

For all the clusters, we choose the celestial coordinates of the cluster centre  $(\alpha, \delta) = (6^h, 0)$ . For the snapshot corresponding to  $z = 0$ , we locate the cluster centre at  $cz = 32,000 \text{ km s}^{-1}$ , similarly to the  $z = 0$  mock catalogues described in Serra et al. (2011).

We have two samples of simulated clusters: 2000 clusters with  $M_{200} \sim 10^{14} h^{-1} M_\odot$  and 50 clusters with  $M_{200} \sim 10^{15} h^{-1} M_\odot$  at  $z = 0$ . By projecting each clusters along three lines of sight, we obtain two samples of 6000 and 150 cluster redshift surveys for the low- and high-mass bins, respectively.

For each mock catalogue, we construct the R-v diagram, the line-of-sight velocity relative to the cluster mean as a function of the projected distance from the cluster centre. The caustic method returns the mass profile estimated from the amplitude of the caustics (see Diaferio 1999; Serra et al. 2011, for further details on the caustic technique).

Figs. 1 and 2 show some examples of the procedure, for the low- and high-mass bins. In both figures, the left and right columns show simulated clusters at  $z = 0.12$  and  $z = 0.19$ , respectively; the upper and lower panels show the R-v diagrams and the mass profiles.

The mass profiles estimated from the caustic amplitude are within the expected uncertainty from the real mass profile within  $\sim 4R_{200}$ . At larger radii, the caustic mass profiles generally flattens, unlike the real mass profile. These regions can include large nearby groups and clusters that would increase the caustic amplitude with increasing radius; however, the caustic technique is designed to favour decreasing amplitudes with increasing radius, to avoid the inclusion of background and foreground systems, as detailed in Diaferio (1999) and Serra et al. (2011). Thus, at radii where the amplitude would increase by an anomalous amount, the algorithm sets the caustic amplitude to zero and the cumulative mass profile flattens.

### 3.3. Radial velocity profiles and the accretion time $t_{\text{inf}}$

The second ingredient of our MAR recipe is the radial velocity profile of the cluster extending to large radii. This piece of information cannot be derived from observations. Therefore, we need to rely on the modelling of clusters in  $N$ -body simulations.

For each cluster, we construct the radial velocity profile by computing the mean radial velocity  $v_{\text{rad}}$  of the particles within individual radial bins. The radial velocity of each particle is  $v_i = [\mathbf{v}_p + H(z_s)a(z_s)\mathbf{r}_{c,i}] \cdot \mathbf{r}_{c,i}/r_{c,i}$ , where, as in the previous section,  $\mathbf{v}_p = \mathbf{u}_p/(1 + z_s)$  is the proper peculiar velocity and  $\mathbf{r}_{c,i}$  is the comoving position vector of the particle from the cluster centre;  $H(z_s)$  and  $a(z_s)$  are the Hubble parameter and the cosmic scale factor at the snapshot redshift  $z_s$ , respectively.

Figure 3 shows the mean and median profiles of the radial velocity of the simulated clusters in our low- and high-mass samples at  $z = 0$  and  $z = 0.44$ . We also show the 68% percentile range of the profile distribution. In the estimate of the velocity profiles, we include both the dark matter and the baryonic particles. The simulated clusters at other redshifts show qualitatively similar results.

By inspecting the radial velocity profile, we can identify three regions: an internal region with radial velocity  $v_{\text{rad}} \approx 0$ , where the matter is moving close to the centre within an isotropic

velocity field; an infall region, where  $v_{\text{rad}}$  becomes negative and indicates an actual infall of matter towards the centre of the cluster; and a Hubble region at radii  $r \gtrsim 4R_{200}$ , where  $v_{\text{rad}}$  becomes positive and the Hubble flow dominates. Broadly speaking, the infall radius  $R_{\text{inf}}$ , defined as the radius where the minimum of  $v_{\text{rad}}$  occurs, is between  $2R_{200}$  and  $3R_{200}$ , independently of the cluster mass and redshift.

We estimate the mean radial velocity profile at discrete values of the radius  $r$ . For the infall velocity  $v_i$  of the shell (Equation 1), we take the radial velocity associated with the bin  $[2 - 2.5]R_{200}$ . The choice of this velocity is consistent with the shell adopted for the estimate of the MAR: the internal radius of the shell is  $R_i = 2R_{200}$ , comparable with the splashback radius (More et al. 2015; Adhikari et al. 2014), and the thickness typically returned by Equation (1) is  $\sim 0.5R_{200}$ . For both bins of cluster mass, this radial bin corresponds to the radial range where the radial velocity profile has its minimum thus capturing the largest contribution to the MAR.

Our prescription for the MAR estimate clearly depends on the choice of both  $R_i$  and  $v_i$ . We will discuss the effect of the value of  $v_i$  on the MAR in Sect. 5.2 below. Here, we show that using the mean infall velocity rather than the infall velocity of each cluster has very little impact on the estimate of the MAR. We compare the spreads of the velocity profiles shown in Fig. 3 with the spreads of the MAR estimates obtained with the mean  $v_i$  and either the three-dimensional mass profiles or the caustic mass profiles that we compute in Sect. 3.4 below and that are shown in Fig. 4.

We use the  $1\sigma$  relative standard deviation of the mean  $\epsilon_x = \sigma_x/(\sqrt{N}\bar{x})$ , where  $\bar{x}$  is the mean of a sample of  $N$  measures of the quantity  $X$ . For the low-mass bin, the infall velocity standard deviation  $\epsilon_{v_i} \approx 1.2\%$  propagates into the standard deviation of the three-dimensional MAR,  $\epsilon_{\text{MAR}_{3D}} \approx 1.1\%$ ; this spread is well within the standard deviation  $\epsilon_{\text{MAR}_{\text{caustic}}} \approx 2.6\%$  of the MAR distribution estimated from the caustic mass profiles. For the high-mass bin, where the number of clusters decreases from 2000 to 50, the velocity standard deviation becomes  $\epsilon_{v_i} \approx 4.0\%$ , which implies an  $\epsilon_{\text{MAR}_{3D}} \approx 7.4\%$  standard deviation of the real three-dimensional MAR; this  $\epsilon_{\text{MAR}_{3D}}$  is much smaller than the  $\epsilon_{\text{MAR}_{\text{caustic}}} \approx 11.4\%$  standard deviation of the MAR estimated from the caustic mass profiles. We thus conclude that assuming the same mean radial velocity profile for every cluster in a given mass and redshift bin does not introduce any systematic bias in the MAR estimate. The uncertainty in the MAR is actually dominated by the uncertainty in the mass profile.

To estimate the MAR of galaxy clusters, we also need the accretion time  $t_{\text{inf}}$  (see Equation 2). Following De Boni et al. (2016), we adopt  $t_{\text{inf}} = 10^9$  yrs, comparable with the dynamical time  $t_{\text{dyn}} = R/\sigma$  for the clusters we consider here, where  $R$  and  $\sigma$  are their size and one-dimensional velocity dispersion, respectively. To see that this value of  $t_{\text{inf}}$  is a reasonable choice, consider a homogeneous spherical system which is  $\alpha$  time denser than the critical density  $3H_0^2/8\pi G$  and thus has mass  $GM = \alpha H_0^2 R^3/2$ . When the system is in virial equilibrium, its potential energy  $W = -3GM^2/5R$  and kinetic energy  $K = 3M\sigma^2/2$  can be combined in the virial relation  $K = |W|/2$  that yields  $GM = 5R\sigma^2/4$ . Therefore,  $t_{\text{dyn}} = R/\sigma = (5/2\alpha)^{1/2} H_0^{-1} \sim 10^9$  yrs when  $\alpha \sim 200$ . The size and the velocity dispersion of the cluster progenitors at earlier times decrease by comparable factors; therefore,  $t_{\text{dyn}}$  remains roughly constant thus justifying the choice  $t_{\text{inf}} = 10^9$  yrs for any cluster at any redshift.

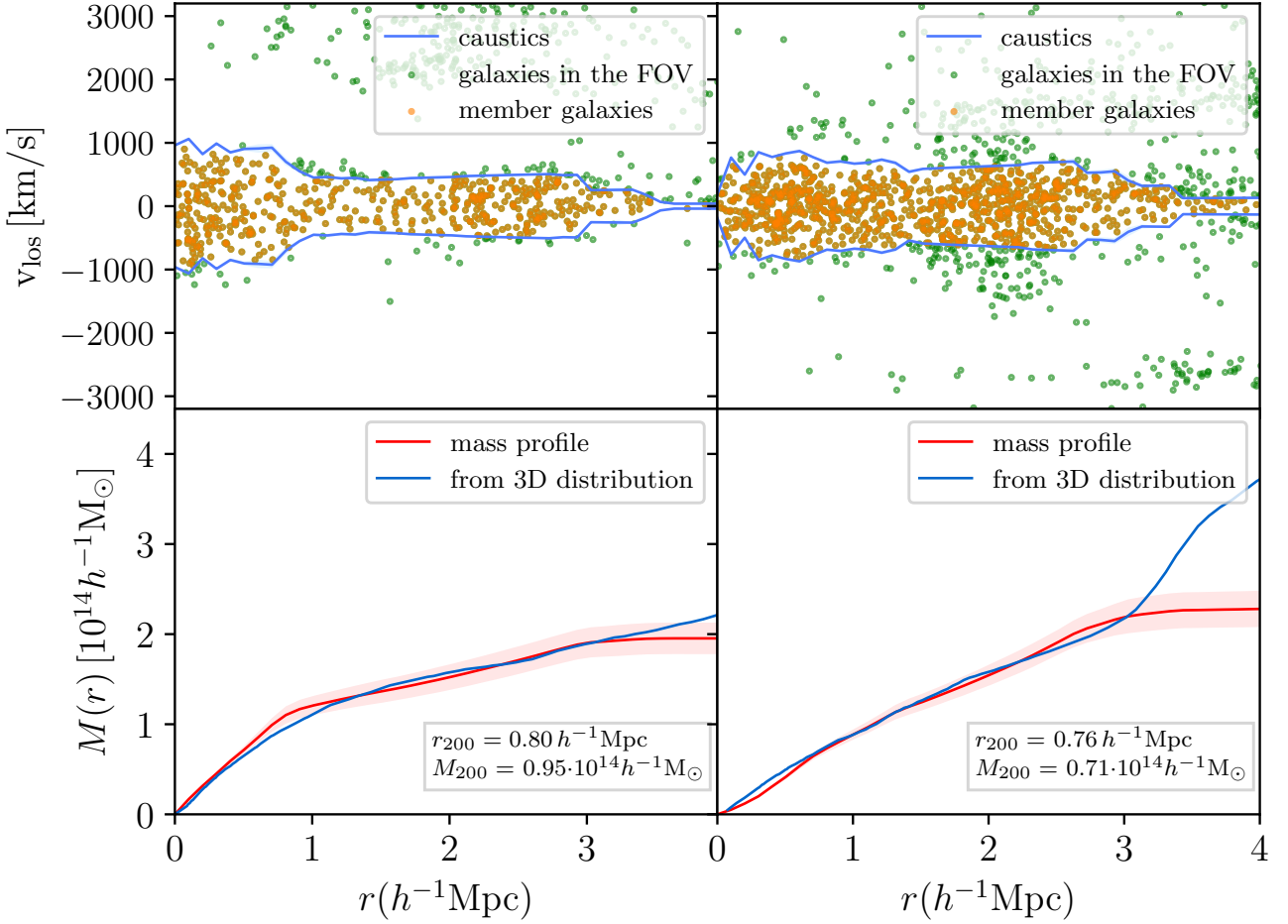


**Fig. 1.** R-v diagram (top panels) and mass profile (bottom panels) of two simulated clusters in the low-mass bin. The left (right) column shows a cluster at  $z = 0.12$  ( $z = 0.19$ ). In the bottom panels, the red (blue) curves show the caustic (real) mass profile. The shaded areas show the 50% confidence level of the caustic location and of the caustic mass profile according to the caustic technique recipe. In the R-v diagrams the areas are present, but very thin.

### 3.4. Estimates of the MAR of simulated clusters

We now apply the caustic technique to each of our mock catalogues to derive the caustic mass profile and to estimate the MAR with our recipe (Equation 2), Sect. 2). We bin the mock catalogues according to the cluster redshift and mass.

As we show with real clusters (Sect. 5), some of the individual R-v diagrams do not support an estimate of the MAR. Our recipe requires that we estimate the mass of the shell of radii  $R_i = 2R_{200}$  and  $(1 + \delta_s)R_i \sim 2.5R_{200}$ . The caustic method estimates this mass from

$$GM_{\text{shell}} = \mathcal{F}_\beta \int_{R_i}^{(1+\delta_s)R_i} \mathcal{A}^2(R) dR, \quad (4)$$

where  $\mathcal{F}_\beta$  is the filling factor (Diaferio 1999; Serra et al. 2011) and  $\mathcal{A}(R)$  is the amplitude of the caustics, namely the vertical separation of the upper and lower caustics at radius  $R$ . At these large radii, a system can return a caustic amplitude  $\mathcal{A}(R) = 0$ , either because of poor sampling (especially in real systems) or because of galaxy-rich background or foreground structures that inhibit the caustic technique from properly identifying the caustic location. In these cases the mass of the shell, and thus the MAR, cannot be estimated.

In the samples of real clusters, we visually inspect the R-v diagrams to identify systems where the caustic technique fails. With the mock catalogues, we adopt an automatic procedure: to be conservative we remove the R-v diagrams where the caustic amplitude  $\mathcal{A}(R) < 100 \text{ km s}^{-1}$  in the range  $[R_i; (1 + \delta_s)R_i]$ . The caustic technique algorithm also prohibits unphysical increases of  $\mathcal{A}(R)$  with increasing  $R$ . This feature of the algorithm is more effective in real clusters than in mock clusters; in fact, the simulated clusters tend to have less sharp separation between the cluster members and the foreground and background galaxies and the caustic amplitude  $\mathcal{A}(R)$  can artificially increase at large  $R$ . Therefore we also remove the R-v diagrams where the caustic amplitude  $\mathcal{A}(R) > 2000 \text{ km s}^{-1}$  in the range  $[R_i; (1 + \delta_s)R_i]$ . This procedure removes 13% and 18% of the R-v diagrams for the low- and high-mass bin, respectively.

In Fig. 4 the red triangles show the median of the caustic MARs of the clusters at each redshift bin. The upper and lower sets of points are relative to the two cluster mass bins, as indicated in the figure. The error bars also show the 68% percentile range of the distribution of the estimated caustic MARs.

To quantify the systematic errors introduced by the projection effects in realistic observations, the blue squares in Fig. 4 show the MAR estimated with the recipe of Sect. 2 but with the

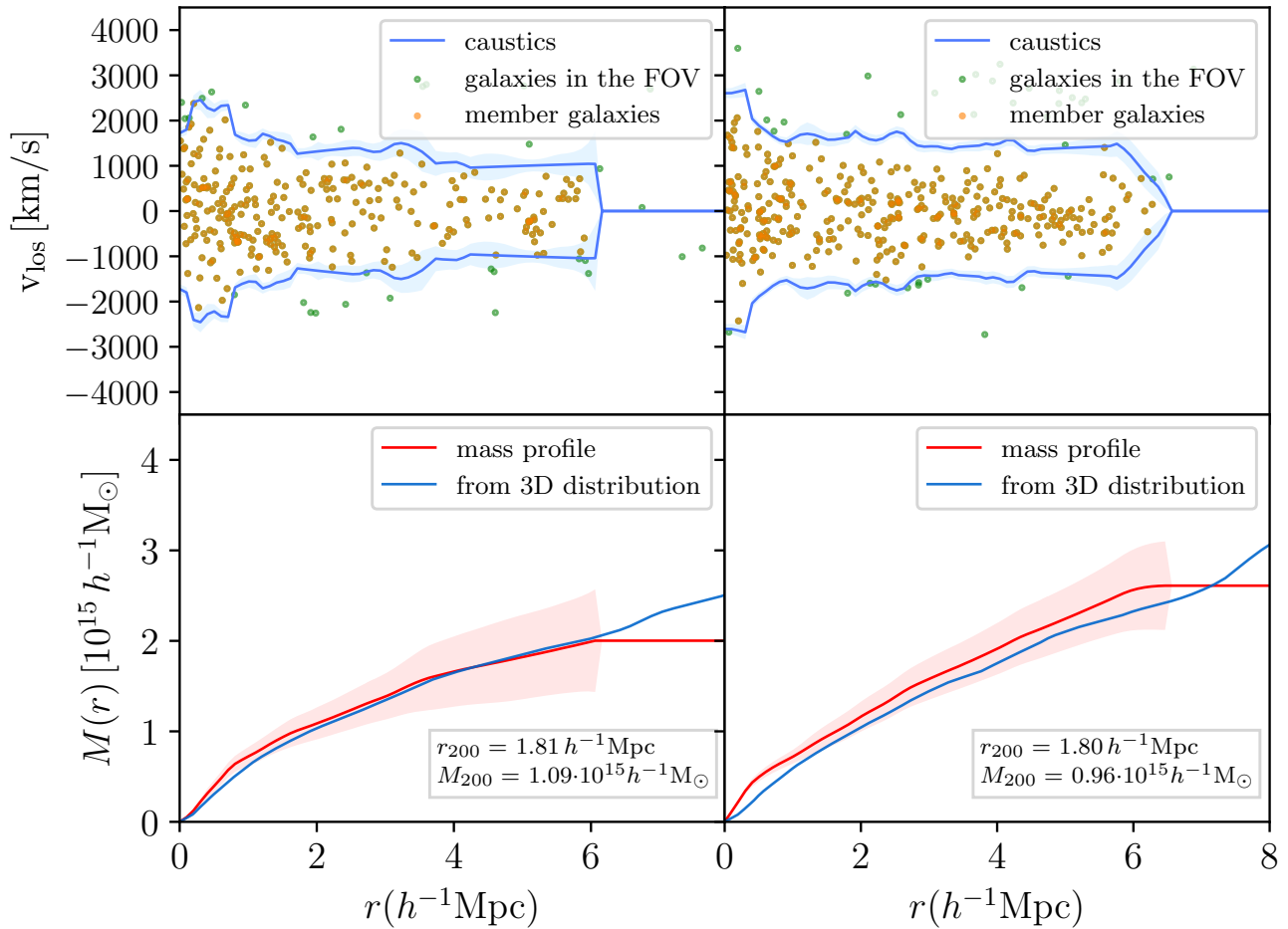


**Fig. 2.** Same as Fig. 1, for two simulated clusters in the high-mass bin.

correct three-dimensional mass profile. The procedure applied to obtain these estimates coincides with the procedure described in De Boni et al. (2016). The agreement between the two estimates of the average MAR is very good at all redshifts and for both mass bins: the average relative difference is  $\lesssim 17\%$ .

The difference between the three-dimensional MAR and the caustic MAR appears in their relative spreads. The relative spreads  $\sigma_{\text{MAR}}/\text{MAR}$  of the MAR obtained with the three-dimensional mass profiles are  $\sim 44\%$  and  $\sim 49\%$  for the low- and the high-mass bin, respectively. In contrast, using the mass profiles estimated with the caustic method, the relative spreads are  $\sim 105\%$  and  $\sim 76\%$ , respectively. These spreads are consistent with the spread of the caustic mass profile around the true mass profile estimated in  $N$ -body simulations (Serra et al. 2011, Fig. 12).

The larger spread in the low-mass bin originates from the fact that in  $N$ -body simulations, less massive systems have less well defined structure in redshift space compared to more massive systems (Diaferio 1999). Consequently, the identification of the caustics is prone to larger random errors. The algorithm takes this effect into account by associating a larger uncertainty with the caustic location and with the mass profile. Redshift space structures are sharper in the real universe (Schmalzing & Diaferio 2000; Casagrande & Diaferio 2006) and applications of the caustic technique to numerous real clusters have indeed shown that the errors in the caustic mass profiles estimated with  $N$ -body

simulations are probably upper limits (Geller et al. 1999; Diaferio et al. 2005; Geller et al. 2013).

Figure 4 demonstrates that the caustic technique should return an unbiased estimate of the median three-dimensional MAR of real clusters at any redshift. In addition, the uncertainties overestimate the spread in the MAR based on three-dimensional mass profiles of a sample of clusters of comparable mass. We conclude that applying our recipe to real clusters should return a robust estimate of their MAR.

#### 4. The catalogues of real clusters

Estimating the MAR of real clusters requires a dense redshift survey of the cluster outer regions. The largest catalogues currently available that satisfy this condition are the Cluster Infall Regions in the Sloan Digital Sky Survey (CIRS) (Rines & Diaferio 2006) and the Hectospec Cluster Survey (HeCS) (Rines et al. 2013). The former catalogue contains clusters at  $z < 0.1$  and the latter contains clusters in the redshift range  $0.1 < z < 0.3$ . These redshift ranges enable us to measure the MAR as a function of redshift.

In Sects. 4.1 and 4.2, we review the main features of the two catalogues; Sect. 4.3 discusses some systematic effects in the selection of the galaxy samples. Sect. 5 describes the estimated MARs.



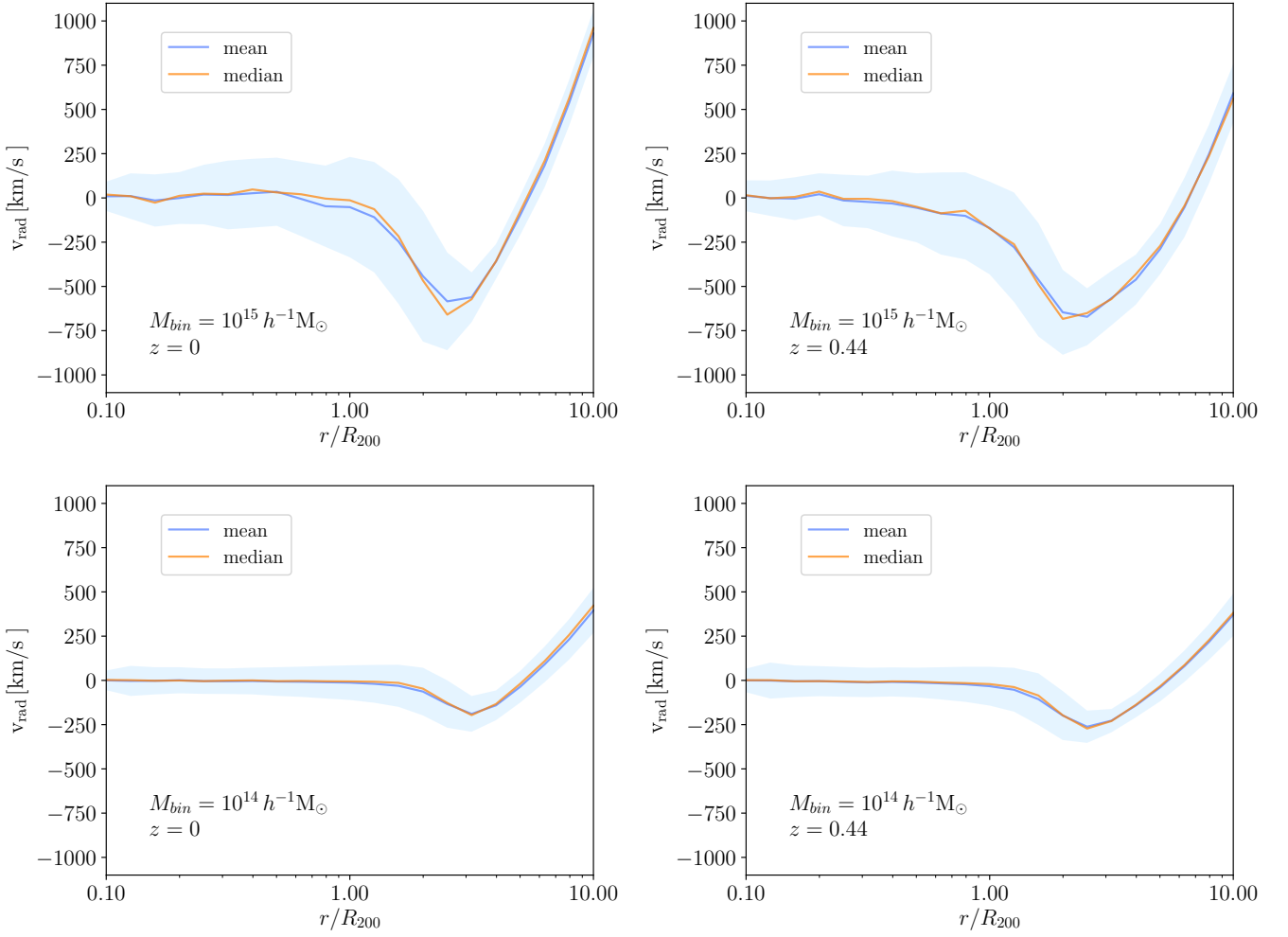


**Fig. 3.** Mean (blue curve) and median (orange curve) profiles of the radial velocity of the particles within the dark matter halos extracted from the simulation for the two mass bins at  $z = 0$  and  $z = 0.44$ , as indicated in the panels. 68% of the profiles of the individual halos lie within the light blue areas.

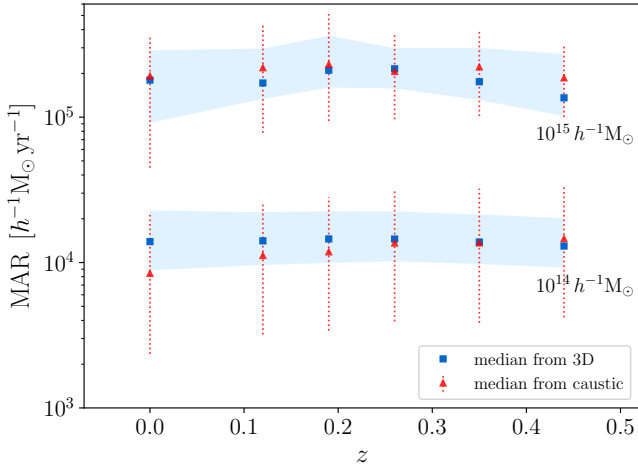


**Fig. 4.** MAR of simulated clusters in the low- (lower set of points) and high- (upper set of points) mass bins. The blue squares and the red triangles show the median MAR based on the three-dimensional and the caustic mass profiles, respectively. The blue shaded areas show the 68% percentile range of the distribution of the MAR derived from the three-dimensional mass profiles; the red error bars show the 68% percentile ranges of the estimates obtained with the caustic mass profiles.

#### 4.1. CIRS

The CIRS project extended the analysis of the CAIRNS survey (Rines et al. 2003), which pioneered the study of the infall region of clusters; CAIRNS used nine nearby galaxy clusters observed by the 2MASS survey (Jarrett 2004), exploiting extensive spectroscopy and near-infrared photometry.

CIRS is based on the Fourth Data Release (DR4) of SDSS, a photometric and spectroscopic wide-area survey at high galactic latitudes and low redshifts (Stoughton et al. 2002). The DR4 includes  $6670 \text{ deg}^2$  of imaging data and  $4783 \text{ deg}^2$  of spectroscopic data (Adelman-McCarthy et al. 2006). It was thus possible to extend the study of infall patterns around clusters initiated by CAIRNS to a larger number of clusters. By matching four X-ray cluster catalogues derived from the ROSAT All Sky Survey (RASS; Voges et al. 1999) to the spectroscopic area covered by the DR4, Rines & Diaferio (2006) obtained the CIRS catalogue, a sample of 74 clusters at  $z < 0.1$ , perfectly suited to the study of infall regions with the caustic technique.

In our analysis, we use the updated catalogues of the CIRS dataset obtained by compiling the SDSS DR14 spectroscopic sample; these new catalogues are now part of the HeCS-omnibus survey (Sohn et al. 2019b). Here, three clusters of the original sample are removed: NGC4636, NGC5846 and Virgo. These



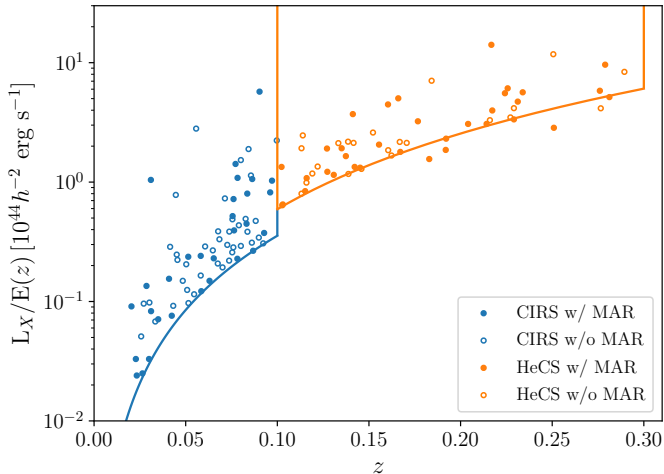


**Fig. 5.** Luminosities of the CIRS (blue points) and HeCS (orange points) clusters as a function of redshift. The superimposed curves show the flux and redshift selection functions of the two catalogues. Filled points refer to the clusters where we can compute an individual MAR.

clusters have redshifts  $< 0.01$  and are poorly sampled. The remaining 71 clusters constitute our CIRS sample. Figure 5 shows the selection function of the CIRS clusters: their X-ray flux limit in the 0.1–2.4 keV band  $3 \times 10^{-12} \text{ erg s}^{-1} \text{ cm}^{-2}$  and their redshift range  $[0, 0.1]$ .

Table 2 lists the celestial coordinates, redshift, size  $R_{200}$ , and the corresponding mass  $M_{200}$ . It also lists the individual MARs estimated with the caustic method and discussed in Sect. 5.1.<sup>2</sup> The blue histogram in Fig. 6 shows the mass distribution of the CIRS clusters. Table 3 lists the medians and percentile ranges of the redshift and mass distributions for both the complete catalogue and the subset of the CIRS clusters for which we estimate the individual MAR.

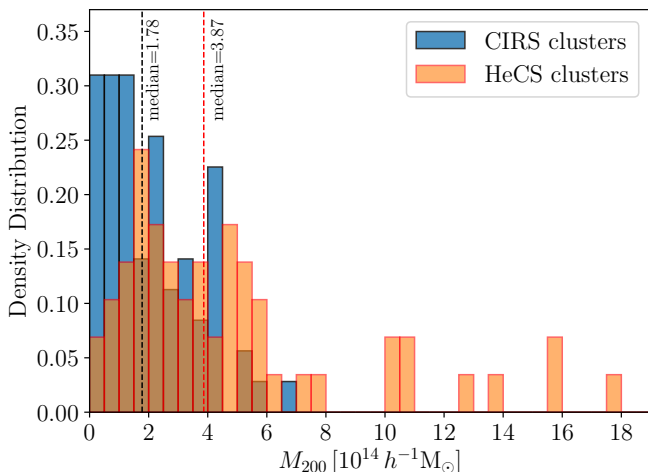


**Fig. 6.** Mass distribution of the CIRS (blue histogram) and HeCS (orange histogram) clusters. The black and red dashed lines show the median masses for the CIRS and HeCS catalogues, respectively.

<sup>2</sup> The properties listed here are derived from the analyses of the updated catalogue of Sohn et al. (2019b); these updated quantities are consistent with the values reported in Rines & Diaferio (2006).

## 4.2. HeCS

HeCS is the first systematic and extensive spectroscopic survey of the infall regions of clusters at  $z \geq 0.1$  (Rines et al. 2013). HeCS takes advantage of the SDSS and RASS surveys. In particular, existing X-ray cluster catalogues based on RASS were used to define flux-limited cluster samples that were then matched to the imaging footprint of the SDSS DR6 (Adelman-McCarthy et al. 2008). Fig. 5 shows the selection function of the HeCS clusters: their X-ray flux limit in the 0.1–2.4 keV band,  $5 \times 10^{-12} \text{ erg s}^{-1} \text{ cm}^{-2}$ , and their redshift range  $[0.1, 0.3]$ . We include four additional clusters below the flux limit but with fluxes  $> 3 \times 10^{-12} \text{ erg s}^{-1} \text{ cm}^{-2}$ .

The imaging footprint of the SDSS DR6 includes 8417 deg<sup>2</sup> of imaging data. The multicolour photometry enabled the selection of candidate cluster members using the red-sequence technique. At  $z \geq 0.1$ , the SDSS spectroscopic survey is not dense enough for accurate measures of the cluster masses with the caustic technique; therefore, the MMT/Hectospec instrument (Fabricant et al. 2005) was used to obtain spectroscopic data for the candidate members. Recently, Sohn et al. (2019b) update the HeCS dataset by using the spectroscopic data of SDSS DR14, and incorporate the new catalogues in the HeCS-omnibus survey.

The HeCS survey contains 58 clusters in the redshift range  $0.1 < z < 0.3$ , for a total amount of 22,680 observed galaxy redshifts, 10,145 of which are cluster members. Each cluster survey typically includes  $\sim 400 - 550$  redshifts; in general, roughly half of these galaxies are cluster members and the remaining galaxies are foreground or background objects.

The orange histogram of Fig. 6 shows the mass distribution of the HeCS cluster sample. This sample includes fewer low-mass clusters than CIRS because it covers a deeper redshift range  $[0.1, 0.3]$ . HeCS also contains more high-mass clusters as a result of the larger survey volume. Due to the extended mass range of the HeCS cluster sample (see Fig. 6), we separate the 58 clusters sorted by mass into two subsamples of 29 clusters each. The low-mass and high-mass samples have median mass  $M_{200} = 1.86 \times 10^{14} h^{-1} M_{\odot}$  and  $M_{200} = 5.61 \times 10^{14} h^{-1} M_{\odot}$ , respectively.

Table 4 lists the HeCS clusters separated into the two subsamples.<sup>3</sup> Table 3 lists the medians and the percentile ranges of the redshift and mass distributions of the entire HeCS catalogue and of its subsamples, including the subsets of clusters for which we estimate the individual MARs in Sect. 5.1.

## 4.3. Effects of the selection of the galaxy samples

### 4.3.1. Photometric completeness

The galaxies in the HeCS clusters are selected according to their red colours, whereas the galaxies in CIRS are from a magnitude-limited survey. Therefore, in principle, unlike CIRS, in HeCS a substantial number of blue galaxies could be missing.

To quantify the impact of these different selections, Fig. 7 shows the colour-magnitude diagram of the two catalogues. We only show the galaxies at projected distance smaller than  $3R_{200}$  from the cluster centre and with line-of-sight velocity  $|v_{\text{los}} - v_{\text{cl}}| < 3000 \text{ km s}^{-1}$ , where  $v_{\text{cl}}$  is the line-of-sight velocity of the cluster. In the right panel, the black solid line shows the fit of Rines et al. (2013) to the red sequence for all the member galaxies in HeCS; on the left panel, the solid line shows the red sequence fit

<sup>3</sup> Similarly to CIRS, the properties listed here are derived from the analyses of the updated catalogue of Sohn et al. (2019b); these updated quantities are consistent with the values reported in Rines et al. (2013).

**Table 2.** CIRS CLUSTERS

cluster	RA [deg]	DEC [deg]	$z$	$R_{200}$ [ $h^{-1}$ Mpc]	$M_{200}$ [ $10^{14} h^{-1} M_{\odot}$ ]	MAR [ $10^3 h^{-1} M_{\odot} \text{yr}^{-1}$ ]
A0085	10.44	-9.46	0.055	$1.216 \pm 0.026$	$4.37 \pm 0.28$	...
A0119	14.06	-1.28	0.044	$1.3008 \pm 0.0084$	$5.31 \pm 0.10$	...
A0160	18.30	15.51	0.043	$0.724 \pm 0.010$	$0.914 \pm 0.037$	...
A0168	18.75	0.28	0.045	$0.703 \pm 0.026$	$0.840 \pm 0.093$	...
A0295	30.54	-1.01	0.042	$0.5253 \pm 0.0049$	$0.349 \pm 0.010$	$10.69 \pm 0.32$
A0602	118.35	29.37	0.060	$1.1903 \pm 0.0014$	$4.124 \pm 0.014$	...
A0671	127.11	30.44	0.050	$1.005 \pm 0.016$	$2.46 \pm 0.12$	...
A0757	138.40	47.76	0.051	$0.505 \pm 0.012$	$0.313 \pm 0.021$	$8.22 \pm 0.86$
A0779	139.93	33.71	0.023	$0.5065 \pm 0.0014$	$0.3079 \pm 0.0026$	$7.705 \pm 0.093$
A0954	151.97	0.58	0.096	$0.660 \pm 0.068$	$0.73 \pm 0.22$	$4.5 \pm 1.6$
A0957	153.43	-0.91	0.046	$0.9558 \pm 0.0016$	$2.108 \pm 0.011$	...
A0971	154.98	40.98	0.092	$1.111 \pm 0.011$	$3.45 \pm 0.10$	...
A1035A	158.10	40.15	0.068	$0.664 \pm 0.041$	$0.72 \pm 0.13$	...
A1035B	158.05	40.28	0.078	$0.7069 \pm 0.0001$	$0.8772 \pm 0.0003$	...
A1066	159.78	5.21	0.069	$0.958 \pm 0.046$	$2.16 \pm 0.31$	...
A1142	165.23	10.51	0.036	$0.641 \pm 0.015$	$0.631 \pm 0.046$	$9.76 \pm 0.97$
A1173	167.38	41.57	0.076	$0.6442 \pm 0.0066$	$0.663 \pm 0.020$	...
A1190	167.96	40.85	0.076	$0.895 \pm 0.013$	$1.779 \pm 0.076$	...
A1205	168.49	2.46	0.076	$0.689 \pm 0.016$	$0.811 \pm 0.056$	$56.0 \pm 5.1$
A1291A	173.09	55.96	0.051	$0.9397 \pm 0.0037$	$2.013 \pm 0.024$	...
A1291B	173.07	56.00	0.059	$1.041 \pm 0.014$	$2.76 \pm 0.11$	...
A1314	173.67	49.08	0.033	$0.803 \pm 0.028$	$1.24 \pm 0.13$	...
A1377	176.85	55.75	0.052	$0.9151 \pm 0.0077$	$1.860 \pm 0.047$	...
A1424	179.42	5.08	0.075	$0.9960 \pm 0.0029$	$2.449 \pm 0.022$	...
A1436	180.05	56.24	0.064	$0.777 \pm 0.055$	$1.15 \pm 0.24$	...
A1552	187.47	11.78	0.086	$1.062 \pm 0.018$	$3.00 \pm 0.15$	...
A1650	194.65	-1.75	0.084	$0.779 \pm 0.024$	$1.18 \pm 0.11$	...
A1663	194.67	-1.73	0.084	$1.201 \pm 0.010$	$4.32 \pm 0.11$	...
A1728	200.58	11.23	0.089	$1.0295 \pm 0.0081$	$2.737 \pm 0.065$	...
A1750	202.69	-1.85	0.085	$1.0691 \pm 0.0086$	$3.055 \pm 0.073$	...
A1767	204.04	59.19	0.071	$1.195 \pm 0.039$	$4.21 \pm 0.41$	...
A1773	205.54	2.25	0.078	$1.179 \pm 0.025$	$4.07 \pm 0.26$	$26.6 \pm 4.5$
A1809	208.29	5.15	0.079	$0.991 \pm 0.038$	$2.42 \pm 0.28$	...
A1885	213.42	43.66	0.089	$0.793 \pm 0.010$	$1.249 \pm 0.049$	...
A2061	230.30	30.58	0.077	$1.154 \pm 0.010$	$3.82 \pm 0.10$	$86.9 \pm 3.4$
A2064	230.24	48.66	0.074	$0.929 \pm 0.014$	$1.985 \pm 0.086$	...
A2067	230.28	30.58	0.077	$1.098 \pm 0.014$	$3.28 \pm 0.12$	...
A2110	234.90	30.71	0.097	$0.707 \pm 0.039$	$0.89 \pm 0.15$	$22.9 \pm 2.7$
A2124	236.25	36.11	0.066	$0.84 \pm 0.15$	$1.44 \pm 0.80$	...
A2142	239.61	27.21	0.089	$1.148 \pm 0.051$	$3.80 \pm 0.51$	$89 \pm 11$
A2149	240.36	54.00	0.065	$0.483 \pm 0.011$	$0.277 \pm 0.020$	$13.82 \pm 0.59$
A2169	243.43	49.07	0.058	$0.655 \pm 0.023$	$0.685 \pm 0.073$	$12.3 \pm 1.7$
A2175	245.10	29.89	0.096	$1.1765 \pm 0.0090$	$4.110 \pm 0.095$	$21.9 \pm 2.6$
A2197	247.46	40.66	0.030	$0.787 \pm 0.014$	$1.163 \pm 0.061$	$26 \pm 12$
A2199	247.12	39.51	0.031	$1.236 \pm 0.024$	$4.50 \pm 0.26$	$75.3 \pm 6.3$
A2244	255.76	33.91	0.099	$1.208 \pm 0.039$	$4.46 \pm 0.43$	...
A2245	255.68	33.52	0.088	$1.159 \pm 0.022$	$3.90 \pm 0.22$	$9.4 \pm 5.3$
A2249	257.44	34.45	0.085	$1.095 \pm 0.052$	$3.28 \pm 0.47$	$53 \pm 22$
A2255	258.10	64.02	0.080	$1.337 \pm 0.019$	$5.94 \pm 0.26$	...
A2399	329.34	-7.82	0.058	$0.968 \pm 0.026$	$2.21 \pm 0.18$	$6.5 \pm 1.4$
A2428	334.09	-9.34	0.084	$0.7523 \pm 0.0074$	$1.063 \pm 0.031$	$27.7 \pm 1.2$
A2593	351.11	14.65	0.042	$0.9809 \pm 0.0084$	$2.271 \pm 0.059$	...
A2670	358.57	-10.44	0.076	$1.1782 \pm 0.0083$	$4.055 \pm 0.085$	$28.7 \pm 1.1$
MKW04	181.12	1.87	0.020	$0.787 \pm 0.020$	$1.151 \pm 0.086$	$5.74 \pm 0.93$
MKW08	220.16	3.47	0.027	$0.584 \pm 0.018$	$0.473 \pm 0.043$	$25.1 \pm 5.3$
MKW11	202.36	11.71	0.023	$0.5737 \pm 0.0004$	$0.4474 \pm 0.0010$	...
MS1306	198.05	-0.98	0.083	$0.8218 \pm 0.0091$	$1.385 \pm 0.046$	$35.15 \pm 0.84$
NGC4325	185.75	10.57	0.025	$0.42 \pm 0.14$	$0.18 \pm 0.18$	...
NGC6107	244.40	35.02	0.032	$0.794 \pm 0.034$	$1.20 \pm 0.15$	$31.3 \pm 7.3$
NGC6338	258.85	57.43	0.029	$0.713 \pm 0.018$	$0.864 \pm 0.066$	$28.6 \pm 2.5$
RXCJ1022p3830	155.60	38.55	0.054	$1.000 \pm 0.013$	$2.429 \pm 0.093$	...
RXCJ1053p5450	163.53	54.85	0.073	$1.0469 \pm 0.0024$	$2.838 \pm 0.020$	...
RXCJ1115p5426	172.27	54.13	0.069	$0.8903 \pm 0.0042$	$1.738 \pm 0.025$	...
RXCJ1210p0523	184.46	3.67	0.077	$1.296 \pm 0.036$	$5.41 \pm 0.45$	$20.0 \pm 2.0$
RXCJ1326p0013	199.83	-0.91	0.084	$0.784 \pm 0.012$	$1.203 \pm 0.056$	...
RXCJ1351p4622	207.90	46.36	0.063	$0.32 \pm 0.39$	$0.084 \pm 0.303$	$13 \pm 11$
RXCJ2214p1350	333.67	13.85	0.026	$0.486 \pm 0.025$	$0.273 \pm 0.042$	$1.95 \pm 0.46$
RXJ0137	24.34	-9.24	0.041	$0.4542 \pm 0.0064$	$0.2253 \pm 0.0096$	$6.21 \pm 0.67$
SHK352	170.41	2.89	0.049	$0.8555 \pm 0.0059$	$1.517 \pm 0.032$	...
Zw1215p0400	184.46	3.68	0.077	$1.404 \pm 0.051$	$6.88 \pm 0.75$	$76.1 \pm 6.4$
Zw1665	125.86	4.37	0.030	$0.5636 \pm 0.0074$	$0.427 \pm 0.017$	...

**Table 3.** CIRS AND HECS SAMPLES

sample	median $z$	68 <sup>th</sup> percentile range [redshift $z$ ]	median $M_{200}$ [ $10^{14}h^{-1}M_{\odot}$ ]	68 <sup>th</sup> percentile range [ $10^{14}h^{-1}M_{\odot}$ ]
all CIRS	0.068	0.033-0.085	1.8	0.64 - 4.0
CIRS with individual MAR	0.064	0.030-0.086	1.1	0.31 - 4.1
all HeCS	0.16	0.12-0.23	3.9	1.5-7.6
all low-mass HeCS	0.14	0.12-0.18	1.9	1.0-2.9
all high-mass HeCS	0.20	0.14-0.25	5.6	4.4-12
low-mass HeCS with individual MAR	0.14	0.12-0.22	2.2	1.2-3.1
high-mass HeCS with individual MAR	0.21	0.16-0.24	5.2	4.3-12

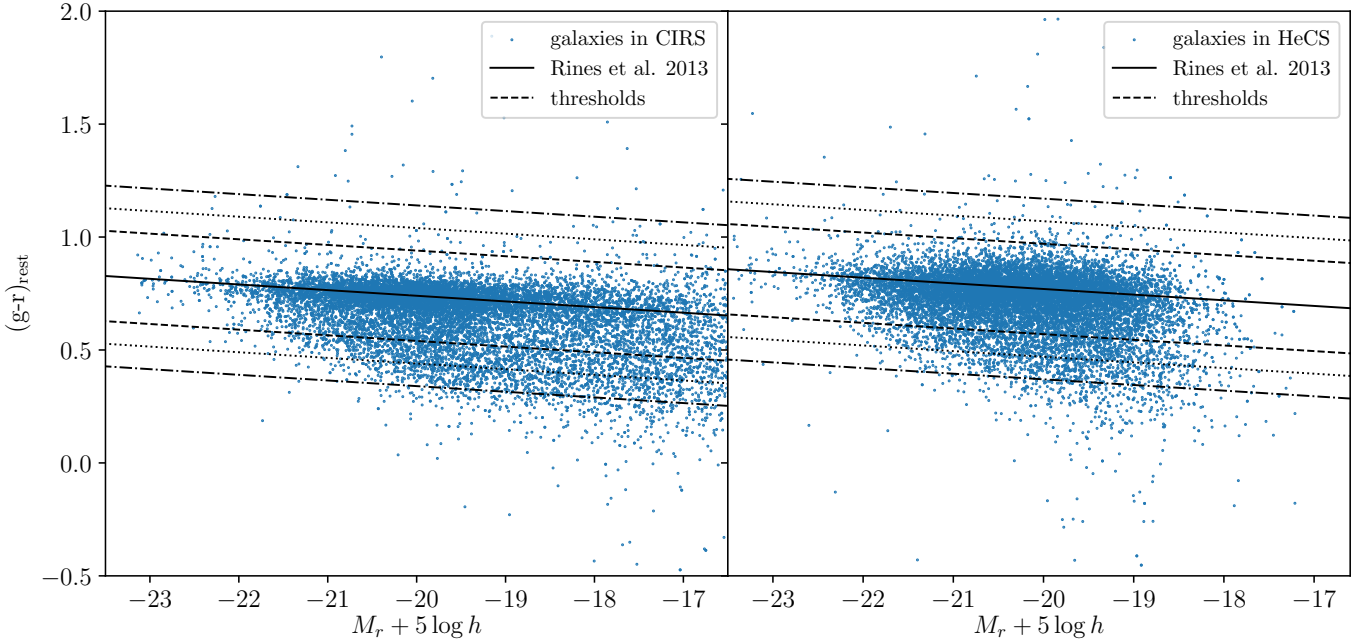


**Fig. 7.**  $(g-r)$  colour-magnitude diagrams of the CIRS (left) and HeCS (right) galaxies, including  $k$ -corrections. The galaxies have a cluster-centric distance smaller than  $3R_{200}$  and line-of-sight velocity  $|v_{los} - v_{cl}| < 3000 \text{ km s}^{-1}$ . The black solid curve in the right panel shows the fit by Rines et al. (2013) derived from the HeCS galaxies. The black dashed, dotted and dash-dotted lines show the  $\pm 0.30, \pm 0.40, \pm 0.50$  shifts of the same fit. In the left panel, the black solid line shows the Rines et al.'s fit with an offset of  $-0.03 \text{ mag}$ . The black dashed, dotted and dash-dotted lines show the  $\pm 0.30, \pm 0.40, \pm 0.50 \text{ mag}$  shifts of this line.

of Rines et al. (2013) shifted by  $-0.03 \text{ mag}$ . The black dashed, dotted and dash-dotted lines show the boundaries of the stripes used for sample selection obtained by changing the intercept of the fit by  $\pm 0.30, \pm 0.40, \pm 0.50 \text{ mag}$ .

Some of the galaxies outside the selection stripes are extremely red. However, they are a tiny minority and they are almost never cluster members (Rines et al. 2013). The impact of red objects can thus be ignored here.

The spatial distribution of the red galaxies peaks within  $R_{200}$ ; the blue galaxy distribution peaks at significantly larger radius. The distributions of the line-of-sight velocities of both red and blue galaxies are centered on zero and are approximately Gaussian; the width of these distributions is smaller for the red galaxies than for the blue galaxies.

Table 5 lists the ratio  $\Xi$  between the number of the blue galaxies outside each of the stripes shown in Fig. 7 and the total number of galaxies in CIRS and HeCS. The fraction of

blue galaxies is  $\lesssim 10\%$  in both catalogues, for any stripe. The relative difference in blue galaxies between CIRS and HeCS,  $\delta_{\Xi} = 1 - \Xi_{\text{HeCS}}/\Xi_{\text{CIRS}}$ , decreases from 29% to 2% from the  $\pm 0.30 \text{ mag}$ - to the  $\pm 0.50 \text{ mag}$ -stripe.

These numbers suggest that HeCS might roughly miss, at most, one third of blue galaxies compared to CIRS. The effect on the caustic location should thus be mild. In addition, the caustic technique locates the caustics by adopting a threshold of the number density distribution of the galaxies in the R-v diagram that is set by the galaxies within  $\sim R_{200}$ . The spatial distribution of the red galaxies peaks within this radius, whereas the blue galaxy distribution peaks further out, as mentioned above.

We prove that missing this fraction of blue galaxies in HeCS does not affect our estimates of the MAR by taking 10 CIRS clusters and randomly removing 35% of the galaxies outside the  $\pm 0.30 \text{ mag}$ -stripe, a slightly larger fraction of the upper limit of  $\delta_{\Xi}$  listed in Table 5. The differences between these caustic mass

**Table 4.** HECS CLUSTERS\*

cluster	RA [deg]	DEC [deg]	$z$	$R_{200}$ [ $h^{-1}$ Mpc]	$M_{200}$ [ $10^{14} h^{-1} M_{\odot}$ ]	$MAR$ [ $10^3 h^{-1} M_{\odot} \text{yr}^{-1}$ ]
A0646	126.34	47.17	0.127	$1.140 \pm 0.014$	$3.84 \pm 0.14$	$43.8 \pm 1.6$
A0655	126.38	47.14	0.127	$1.049 \pm 0.048$	$3.00 \pm 0.41$	$40.8 \pm 7.4$
A0667	127.02	44.80	0.145	$0.9173 \pm 0.0005$	$2.0384 \pm 0.0032$	$22.519 \pm 0.027$
A0689	129.36	14.97	0.279	$0.740 \pm 0.017$	$1.220 \pm 0.084$	$82.0 \pm 4.4$
A0750	137.23	11.02	0.164	$0.967 \pm 0.051$	$2.43 \pm 0.39$	$53 \pm 14$
A0990	155.90	49.16	0.141	$0.965 \pm 0.070$	$2.36 \pm 0.51$	...
A1033	157.91	35.06	0.122	$0.9330 \pm 0.0061$	$2.100 \pm 0.041$	...
A1068	160.19	39.93	0.138	$0.517 \pm 0.044$	$0.362 \pm 0.092$	...
A1132	164.60	56.79	0.135	$1.0028 \pm 0.0030$	$2.639 \pm 0.024$	$102.6 \pm 1.1$
A1201	168.22	13.42	0.167	$1.01 \pm 0.14$	$2.79 \pm 1.16$	$53 \pm 21$
A1204	168.33	17.59	0.170	$0.641 \pm 0.078$	$0.71 \pm 0.26$	...
A1235	170.84	19.59	0.103	$0.789 \pm 0.019$	$1.246 \pm 0.091$	$31.7 \pm 2.5$
A1302	176.20	67.43	0.116	$1.033 \pm 0.021$	$2.83 \pm 0.17$	$77 \pm 10$
A1361	175.91	46.35	0.116	$0.8431 \pm 0.0070$	$1.540 \pm 0.038$	...
A1366	176.22	67.40	0.116	$0.855 \pm 0.031$	$1.61 \pm 0.18$	$118 \pm 25$
A1423	179.28	33.62	0.214	$1.085 \pm 0.020$	$3.61 \pm 0.20$	$80.9 \pm 4.8$
A1902	215.44	37.29	0.163	$1.088 \pm 0.036$	$3.46 \pm 0.35$	...
A1918	216.26	63.16	0.140	$0.481 \pm 0.027$	$0.293 \pm 0.049$	...
A1930	218.18	31.58	0.131	$0.8373 \pm 0.0094$	$1.529 \pm 0.051$	$22.0 \pm 1.4$
A1978	222.79	14.63	0.146	$0.828 \pm 0.014$	$1.502 \pm 0.075$	...
A2055	229.70	6.24	0.103	$0.852 \pm 0.034$	$1.57 \pm 0.19$	$29.4 \pm 5.6$
A2187	246.05	41.23	0.183	$0.724 \pm 0.030$	$1.04 \pm 0.13$	$67.5 \pm 9.4$
A2259	260.04	26.63	0.160	$0.88 \pm 0.13$	$1.84 \pm 0.83$	...
A2261	260.60	32.03	0.225	$0.987 \pm 0.049$	$2.74 \pm 0.41$	$162 \pm 28$
RXJ1720	260.04	26.62	0.160	$0.8853 \pm 0.0049$	$1.858 \pm 0.031$	$35.5 \pm 1.1$
RXJ2129	322.42	0.08	0.234	$1.062 \pm 0.013$	$3.45 \pm 0.13$	$33.2 \pm 1.5$
Zw1478	119.98	54.00	0.103	$0.674 \pm 0.029$	$0.78 \pm 0.10$	...
Zw3179	156.48	12.70	0.142	$0.73 \pm 0.13$	$1.04 \pm 0.55$	$26.1 \pm 5.2$
Zw8197	259.34	56.66	0.113	$0.984 \pm 0.053$	$2.45 \pm 0.39$	...
A0267	28.18	0.98	0.229	$1.2290 \pm 0.0028$	$5.320 \pm 0.036$	...
A0697	130.76	36.37	0.282	$1.62 \pm 0.10$	$12.7 \pm 2.4$	$201 \pm 69$
A0773	139.50	51.75	0.218	$1.6849 \pm 0.0056$	$13.54 \pm 0.14$	$250.1 \pm 4.4$
A0795	141.01	14.15	0.137	$1.140 \pm 0.013$	$3.89 \pm 0.13$	$41.8 \pm 1.7$
A0963	154.31	39.03	0.204	$1.183 \pm 0.070$	$4.62 \pm 0.82$	$230 \pm 47$
A0980	155.61	50.12	0.156	$1.195 \pm 0.091$	$4.6 \pm 1.0$	$36.5 \pm 8.1$
A1246	171.06	21.47	0.192	$1.162 \pm 0.062$	$4.34 \pm 0.70$	$127 \pm 49$
A1413	178.83	23.41	0.141	$1.201 \pm 0.095$	$4.6 \pm 1.1$	$71 \pm 44$
A1437	178.83	3.33	0.133	$1.607 \pm 0.065$	$10.8 \pm 1.3$	...
A1553	187.67	10.56	0.167	$1.2094 \pm 0.0020$	$4.768 \pm 0.024$	...
A1682	196.72	46.53	0.227	$1.3886 \pm 0.0006$	$7.654 \pm 0.009$	...
A1689	197.90	-1.32	0.184	$1.871 \pm 0.013$	$17.95 \pm 0.36$	...
A1758	203.15	50.56	0.276	$1.512 \pm 0.036$	$10.38 \pm 0.75$	$109.8 \pm 6.9$
A1763	203.83	41.00	0.231	$1.55 \pm 0.14$	$10.7 \pm 2.9$	$87 \pm 30$
A1835	210.27	2.87	0.252	$1.758 \pm 0.012$	$15.94 \pm 0.33$	...
A1914	216.51	37.84	0.166	$1.257 \pm 0.023$	$5.35 \pm 0.30$	$265 \pm 46$
A2009	225.09	21.37	0.152	$1.272 \pm 0.040$	$5.47 \pm 0.52$	...
A2034	227.52	33.47	0.113	$1.3628 \pm 0.0037$	$6.487 \pm 0.052$	...
A2050	229.07	0.07	0.119	$1.3010 \pm 0.0033$	$5.673 \pm 0.043$	...
A2069	231.04	29.87	0.114	$1.32 \pm 0.16$	$5.9 \pm 2.1$	...
A2111	234.93	34.41	0.230	$1.3597 \pm 0.0050$	$7.207 \pm 0.079$	$171.6 \pm 3.7$
A2219	250.06	46.71	0.226	$1.776 \pm 0.056$	$16.0 \pm 1.5$	$244 \pm 67$
A2396	328.91	12.50	0.192	$1.267 \pm 0.018$	$5.61 \pm 0.24$	$82.9 \pm 5.5$
A2631	354.40	0.25	0.277	$1.494 \pm 0.011$	$10.02 \pm 0.22$	...
A2645	335.32	-9.03	0.251	$1.101 \pm 0.039$	$3.91 \pm 0.41$	$66 \pm 21$
MS0906	137.28	10.94	0.177	$1.2247 \pm 0.0034$	$4.998 \pm 0.041$	$48.59 \pm 0.50$
RXJ1504	226.02	-2.81	0.216	$1.15 \pm 0.12$	$4.3 \pm 1.4$	$63 \pm 20$
Zw2701	148.25	51.85	0.215	$1.116 \pm 0.034$	$3.92 \pm 0.36$	...
Zw3146	155.91	4.19	0.290	$1.200 \pm 0.076$	$5.26 \pm 0.99$	...

\*The upper (lower) part of the table lists the low-mass (high-mass) subsample of the HeCS clusters.

**Table 5.** RELATIVE DIFFERENCE OF BLUE GALAXIES IN CIRS AND HeCS

stripe	$\Xi_{\text{CIRS}}$	$\Xi_{\text{HeCS}}$	$\delta\Xi$
$\pm 0.30$ mag	0.1072	0.0764	0.287
$\pm 0.40$ mag	0.0387	0.0319	0.176
$\pm 0.50$ mag	0.0150	0.0147	0.020

profiles and the original profiles are within the uncertainties of the caustic technique, and are thus statistically indistinguishable.

Our conclusion is further supported by Rines et al. (2013). They present a case study of three HeCS clusters: with additional spectroscopic observations including blue galaxies, they can quantify how these galaxies can affect the estimate of the velocity dispersion and the dynamical mass. They find that a small fraction of blue galaxies are actual cluster members and their inclusion only increases the velocity dispersion by 0.3%. Rines et al. (2013) conclude that targeting the galaxies on the red-sequence alone does not produce any bias on the velocity dispersion and the mass estimates.

#### 4.3.2. Spectroscopic completeness

In general, the spectroscopic completeness, namely the ratio between the number of galaxies with spectroscopic measurement and the number of galaxies with photometric measurement, can decrease with increasing distance from the cluster centre. In CIRS, the spectroscopic completeness could be affected by the edges of the footprint of SDSS, whereas in HeCS, spectroscopic redshifts are only available within 30 arcmin from the cluster centre. Hence, the spectroscopic measurements can be incomplete at large radii. For the caustic method, this incompleteness can cause an underestimate of the caustic amplitude and thus an underestimate of the cluster mass and of the MAR. However, when the sample is too sparse, the caustic method refrains from locating the caustics and returns no mass estimates. In contrast, if the incompleteness is not too severe to prevent the location of the caustics, the underestimate of the mass might be within the caustic mass uncertainty. At the end of this section, we confirm that this is indeed the case for the CIRS and HeCS clusters.

We are now first concerned with the fact that the spectroscopic incompleteness could differently affect the two catalogues and thus differently bias our MAR estimates. We show that this case does not occur, and that the spectroscopic incompleteness is comparable in the two CIRS and HeCS samples.

The left panel of Fig. 8 shows the ratio  $\mathcal{P} = \mathcal{P}_{[2,2.5]}/\mathcal{P}_{[0,1]}$  between the numbers of galaxies with photometric measures in the range  $r/R_{200} \in [2, 2.5]$  and in the range  $r/R_{200} \in [0, 1]$ . The right panel shows the ratio  $\mathcal{S} = \mathcal{S}_{[2,2.5]}/\mathcal{S}_{[0,1]}$  of the numbers of galaxies with spectroscopic redshift in the same two regions. Blue and orange points show the CIRS and HeCS clusters, respectively. The ratios  $\mathcal{P}$  and  $\mathcal{S}$  of each cluster are computed with the galaxies brighter than  $M_r = -20$ . This limit is  $\sim M_r^* + 1$ , where  $M_r^* \approx -21$  is the characteristic red-band magnitude of the Schechter luminosity function, as indicated by photometric studies of A2029 and Coma (Sohn et al. 2017). The left panel shows that, on average, the photometric samplings of the CIRS and HeCS surveys in the central and outer regions of the clusters are comparable:  $\langle \mathcal{P} \rangle = 0.99 \pm 0.61$  and  $\langle \mathcal{P} \rangle = 0.97 \pm 0.27$  for CIRS and HeCS, respectively. A similar result holds for the spectroscopic samplings:  $\langle \mathcal{S} \rangle = 0.65 \pm 0.30$  and  $\langle \mathcal{S} \rangle = 0.73 \pm 0.22$  for CIRS and HeCS, respectively.

The values of the ratio  $\mathcal{S} < 1$  suggest that the spectroscopic completeness might decrease with distance from the cluster centre. In fact, Fig. 9 shows the spectroscopic completenesses  $\mathcal{S}_{[0,1]}/\mathcal{P}_{[0,1]}$  and  $\mathcal{S}_{[2,2.5]}/\mathcal{P}_{[2,2.5]}$  in the central and outer regions of the clusters, and confirms a spectroscopic incompleteness at large radii. Nevertheless, the spectroscopic completenesses in the central and outer regions are comparable in the two catalogues. In the centre, CIRS and HeCS have mean spectroscopic completeness  $0.75 \pm 0.12$  and  $0.65 \pm 0.15$ , respectively. In the outer region, the mean completenesses are  $0.53 \pm 0.19$  and  $0.49 \pm 0.15$ . We obtain similar results by considering the subsample of clusters for which, as we illustrate in the next section, we estimate the MAR individually. The similarity of the ratios  $\mathcal{P}$  and  $\mathcal{S}$  of CIRS and HeCS in Fig. 8 shows that the comparable completenesses are not a fluke originating from different photometric samplings in the central and outer regions of the two catalogues.

Based on these results, we conclude that the spectroscopic incompleteness as a function of radius is present in our samples, but it might similarly bias our MAR estimates of the CIRS and HeCS clusters. This conclusion is further supported by the fact that the fraction of clusters with null amplitude beyond  $2R_{200}$  is  $\sim 50\%$  in both catalogues, as we show in the next section. In turn, these fractions are larger than the fractions  $\sim 13 - 18\%$  found for the simulated clusters (Sect. 3.4).

We now quantify the possible systematic error resulting from the spectroscopic incompleteness as a function of radius. We create mock catalogues by stacking the simulated clusters at  $z = 0.12$ , the intermediate redshift between the average redshifts of the CIRS and HeCS clusters. We stack all the 141 clusters of the high-mass bin, whereas we stack a random sample of only 35 clusters of the low-mass bins, to limit the computational time. The R-v diagrams of these two stacked clusters contain  $\sim 50,000$  particles, and simulate catalogues that are spectroscopically complete. We also create mock catalogues by randomly removing some particles within  $r/R_{200} = 1$  and within the range  $r/R_{200} \in [2, 2.5]$  to simulate the spectroscopic incompleteness as a function of radius. We consider two undersampled catalogues: in the first catalogue, we remove 25% and 47% of the particles in the central and outer regions, respectively; in the second catalogue, we remove 35% and 51% of the particles in the two regions. These fractions are chosen accordingly to the mean spectroscopic incompleteness estimated above for the CIRS and HeCS clusters.

The undersampled mock catalogues return mass and MAR estimates consistent with the estimates obtained from the complete catalogues: with the undersampled catalogues, the mass  $M_{200}$  is underestimated by  $\sim 13\%$ , whereas the MARs is overestimated by  $\sim 22\%$ , on average. Both values are within the uncertainties of the estimates obtained from the complete catalogues and are thus statistically indistinguishable. The MAR is, on average, overestimated rather than underestimated, as one might have naively expected; this overestimate confirms that the spectroscopic incompleteness as a function of radius in the CIRS and HeCS clusters can generate statistical fluctuations on the MAR estimates rather than a systematic error.

## 5. Measure of the mass accretion rate of real clusters

Here, we discuss our estimates of the MAR of individual clusters (Sect. 5.1) and the average MAR of the cluster samples (Sect. 5.2) as a function of mass and redshift.

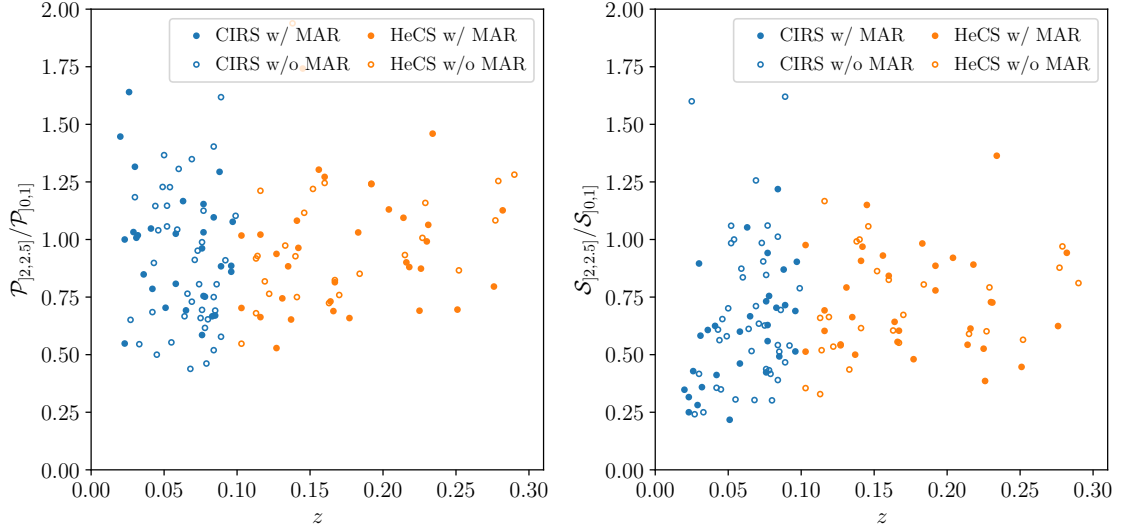


**Fig. 8.** Left panel: ratio between the numbers of galaxies with photometric data in the range  $r/R_{200} \in [2, 2.5]$  and within  $r/R_{200} = 1$  within each cluster, against the cluster redshift. Right panel: ratio between the numbers of galaxies with spectroscopic redshifts within the same regions. Blue and orange points show the CIRS and HeCS clusters, respectively. Solid points show the clusters for which we estimate the individual MAR.

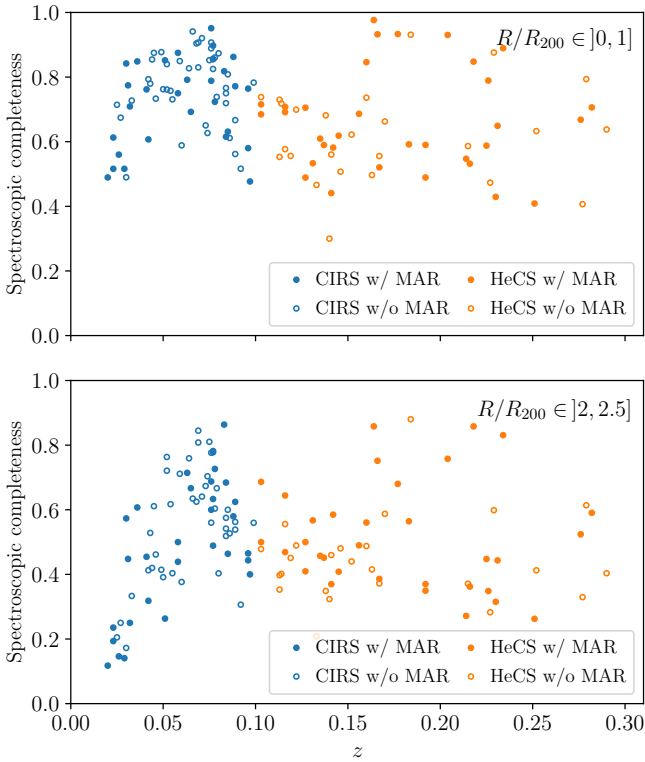


**Fig. 9.** Spectroscopic completeness of the CIRS (blue points) and HeCS (orange points) clusters, against their redshifts, within  $r/R_{200} = 1$  from the cluster centre (upper panel) and within the range  $r/R_{200} \in [2, 2.5]$  (lower panel). Solid points show the clusters for which we estimate the individual MAR.

### 5.1. Individual MARs

As anticipated in Sects. 4.1 and 4.2, we only estimate the individual MAR of a subset of clusters, selected by visually inspecting their R-v diagrams. In fact, we remove (i) the clusters

whose caustic amplitude shrinks to zero within the infalling mass shell, and (ii) the clusters whose caustics have unphysical spikes. These cases usually occur in the presence of galaxy-rich background or foreground structures that prevent the caustic technique algorithm from properly identifying the caustic location. This procedure is similar to the automatic procedure adopted for the mock catalogues in Sect. 3.4. Visual inspection identifies 30 clusters (out of 71) for the CIRS sample. We recover subsamples of 18/29 and 16/29 clusters, respectively, for the low- and high-mass HeCS samples.

The initial infall velocity  $v_i$  entering Equation (1) depends on the cluster mass and redshift. Rather than considering the mass and redshift of each cluster, we consider the same  $v_i$  for all the clusters within each sample. We thus estimate the value of  $v_i$  appropriate for the median redshift and the median mass of each cluster sample.

The median mass and redshift of the CIRS subsample are  $M_{200} = 1.1 \times 10^{14} h^{-1} M_{\odot}$  and  $z = 0.064$  (Table 3). The closest redshifts of the simulated snapshot are  $z = 0$  and  $z = 0.12$ . We thus estimate  $v_i$  appropriate for the CIRS median mass with three linear interpolations on the simulation information. For each of the two simulated samples of mass  $10^{14}$  and  $10^{15} h^{-1} M_{\odot}$ , we first interpolate between the two median masses at redshifts  $z = 0$  and  $z = 0.12$  listed in Table 1 to estimate the appropriate median masses at  $z = 0.064$ ,  $M_{0.064}^1$  and  $M_{0.064}^2$ . The second interpolation returns the velocities appropriate for  $z = 0.064$ ,  $v_{0.064}^1$  and  $v_{0.064}^2$ , for each of the two simulated samples: for each sample, we consider the radial velocity profiles at the two redshifts  $z = 0$  and  $z = 0.12$  and consider the value of the velocity at the single radius lying in the range  $[2 - 2.5] R_{200}$ ;  $v_{0.064}^1$  and  $v_{0.064}^2$  derive from the interpolation between the two values at redshifts  $z = 0$  and  $z = 0.12$  for each sample. Finally, to obtain  $v_i$  appropriate for the median mass  $M_{200} = 1.1 \times 10^{14} h^{-1}$  at  $z = 0.064$ , we interpolate between the two median masses  $M_{0.064}^1$  and  $M_{0.064}^2$  and the two velocities  $v_{0.064}^1$  and  $v_{0.064}^2$ . We find  $v_i = -170 \pm 3 \text{ km s}^{-1}$ .

For the sake of completeness, we also estimate the uncertainty on  $v_i$  with an analogous interpolation based on the profile of the standard deviation of the mean radial velocity profile; the standard deviation is comparable to the 68% percentile range



shown by the shaded bands in Fig. 3. As discussed in Sect. 3.3, the spread on  $v_i$  is roughly a factor three smaller than the uncertainty on the MAR derived from the caustic technique and does not generate any bias on the MAR itself. Therefore, we ignore the uncertainty on  $v_i$  when computing the shell thickness (Equation 1).

For the two HeCS subsamples, we adopt the same procedure. The median mass and redshift of the low-mass HeCS subsample are  $M_{200} = 2.2 \times 10^{14} h^{-1} M_\odot$  and  $z = 0.14$  (Table 3), and we use the snapshots of the simulation at redshifts  $z = 0.12$  and  $z = 0.19$ . We find  $v_i = -288 \pm 8 \text{ km s}^{-1}$ .

For the high-mass HeCS subsample, the median mass is  $M_{200} = 5.2 \times 10^{14} h^{-1} M_\odot$  and the median redshift is  $z = 0.21$  (Table 3). The closest redshifts of the simulated snapshots are  $z = 0.19$  and  $z = 0.26$ . We thus find  $v_i = -566 \pm 19 \text{ km s}^{-1}$ .

The uncertainty in the MAR only depends on the uncertainty  $\sigma_{M_{\text{shell}}}$  on the mass  $M_{\text{shell}}$  of the infalling shell, because we adopt a value for  $t_{\text{inf}}$  without an uncertainty. The caustic method estimates the mass profile from the caustic amplitudes  $\mathcal{A}_i$  measured at a set of radii  $r_i$ . The mass  $M_i$  of the  $i$ -th shell is proportional to  $\mathcal{A}_i^2$ . According to Diaferio (1999) and Serra et al. (2011), we thus estimate the uncertainty on the mass of the infalling shell as

$$\sigma_{M_{\text{shell}}} = \sum 2 M_i \frac{\sigma_{\mathcal{A}_i}}{\mathcal{A}_i}, \quad (5)$$

where the sum extends over the shells of the caustic mass profile within the infalling shell, and  $\sigma_{\mathcal{A}_i}$  is the uncertainty on the caustic amplitude of the  $i$ -th shell; this uncertainty increases with decreasing ratio between the number of galaxies within the caustics and the number of galaxies within the R-v diagram at each radius  $r_i$ . Below, we find that the relative uncertainties of the individual MARs are 25% at most; they mostly derive from (1) the assumption of spherical symmetry, and (2) the presence of very populated R-v diagrams that make the location of the caustics challenging.

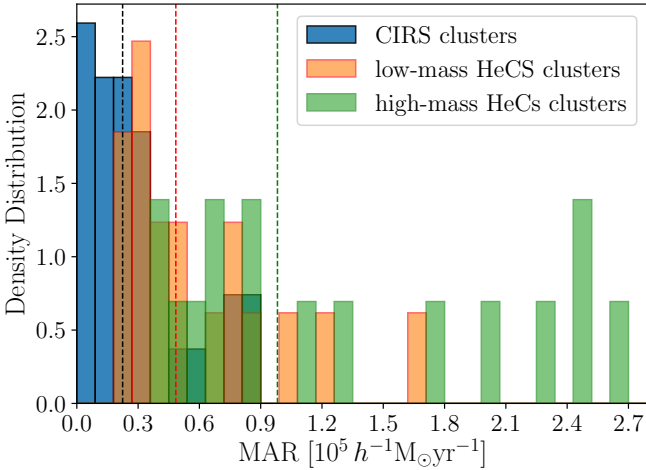


**Fig. 10.** Distributions of the individual MARs. The blue, orange and green histograms refer to the CIRS, low-mass HeCS and high-mass HeCS clusters, respectively. The dashed lines with the same colours show the median MAR of each sample.

Tables 2 and 4 list the individual MARs and Fig. 10 shows the distributions of the individual MARs of our three cluster subsamples. The density distributions are normalized to unity for an easier comparison. The blue, orange and green histograms refer

to the CIRS, low-mass HeCS and high-mass HeCS clusters, respectively; the same colours are used for the vertical dashed lines showing their median MAR. The distributions generally show a peak at small MARs and an extended tail of large MARs. In general, the small and large MARs are associated with low- and high-mass clusters, respectively.

Figures 11 and 12 show R-v diagrams and cumulative mass profiles for six sample clusters. In all the panels, the black dashed line shows the inner radius of the infalling shell; the red dashed line shows the outer radius of the shell (Equation 1). In the two figures, the mass of the cluster,  $M_{200}$ , increases from top to bottom. More massive systems tend to be surrounded by larger amounts of mass and the caustic amplitude decreases more slowly with radius. Consequently, we expect that the mass of the infalling shell, and thus the MAR, correlates with  $M_{200}$ .

Figure 13 shows the correlation between  $M_{200}$  and the MAR. There is also, as expected, a correlation with redshift. The positive correlation with redshift and  $M_{200}$  is clearly expected in the hierarchical clustering scenario where more massive halos lie in higher density regions and they are surrounded by larger amounts of mass (Bardeen et al. 1985; Lacey & Cole 1993; McBride et al. 2009; Fakhouri et al. 2010; van den Bosch et al. 2014). Similarly, halos with comparable masses are expected to have larger MARs at larger redshifts. The correlations are statistically significant according to Kendall's test: the coefficients,  $\tau$ , are 0.522 and 0.520 for the MAR vs  $M_{200}$  and vs  $z$ , respectively, with corresponding significance levels  $p_{M_{200}} = 1.1 \cdot 10^{-9}$  and  $p_z = 1.4 \cdot 10^{-9}$ .

To compare these measures with our simulated clusters, we consider each simulated cluster sample at the four redshifts  $z = 0.0, 0.12, 0.19$ , and  $0.26$ , and separate each sample into four mass bins; these splittings yield 16 subsamples for each of the  $10^{14}$  and  $10^{15} h^{-1} M_\odot$  sample of simulated clusters. The empty circles in Fig. 13 show the median MARs of these 32 subsamples. The  $\Lambda$ CDM expectations appear fully consistent with our measures.

We close this section with a brief comment about two specific clusters: A750 and A1758. In agreement with Rines et al. (2013), we find that the galaxies in the redshift catalogue of A750 belong to two different clusters at different redshifts: A750 at  $z = 0.164$ , and MS0906 at  $z = 0.177$ . The caustic technique successfully identifies the two clusters and estimates the two MARs separately. Their individual MARs are listed in Table 4. A750 belongs to the low-mass HeCS sample, whereas MS0906 is in the high-mass sample.

Similarly, a weak lensing analysis, based on  $B$  and  $V$  passbands images of A1758 at redshift  $z = 0.28$ , by Ragozzine et al. (2011), suggests that this cluster is a system of four gravitationally bound substructures currently undergoing two separate mergers. The mass estimate derived by the caustic technique is not affected by the presence of substructures (Diaferio 1999) and we can thus estimate the MAR of A1758 without any particular precaution (Table 4).

## 5.2. Average MAR

Figure 14 shows the median of the individual MARs as a function of redshift. The green filled circle at redshift  $z = 0.064$  shows the median MAR of the CIRS clusters; the green filled circles at redshift  $z = 0.14$  and  $z = 0.21$  show the median MARs of the two HeCS subsamples. We plot each green circle at the median redshift of the subsample. The number close to each of them shows the median mass of each sample in units of  $h^{-1} M_\odot$ .



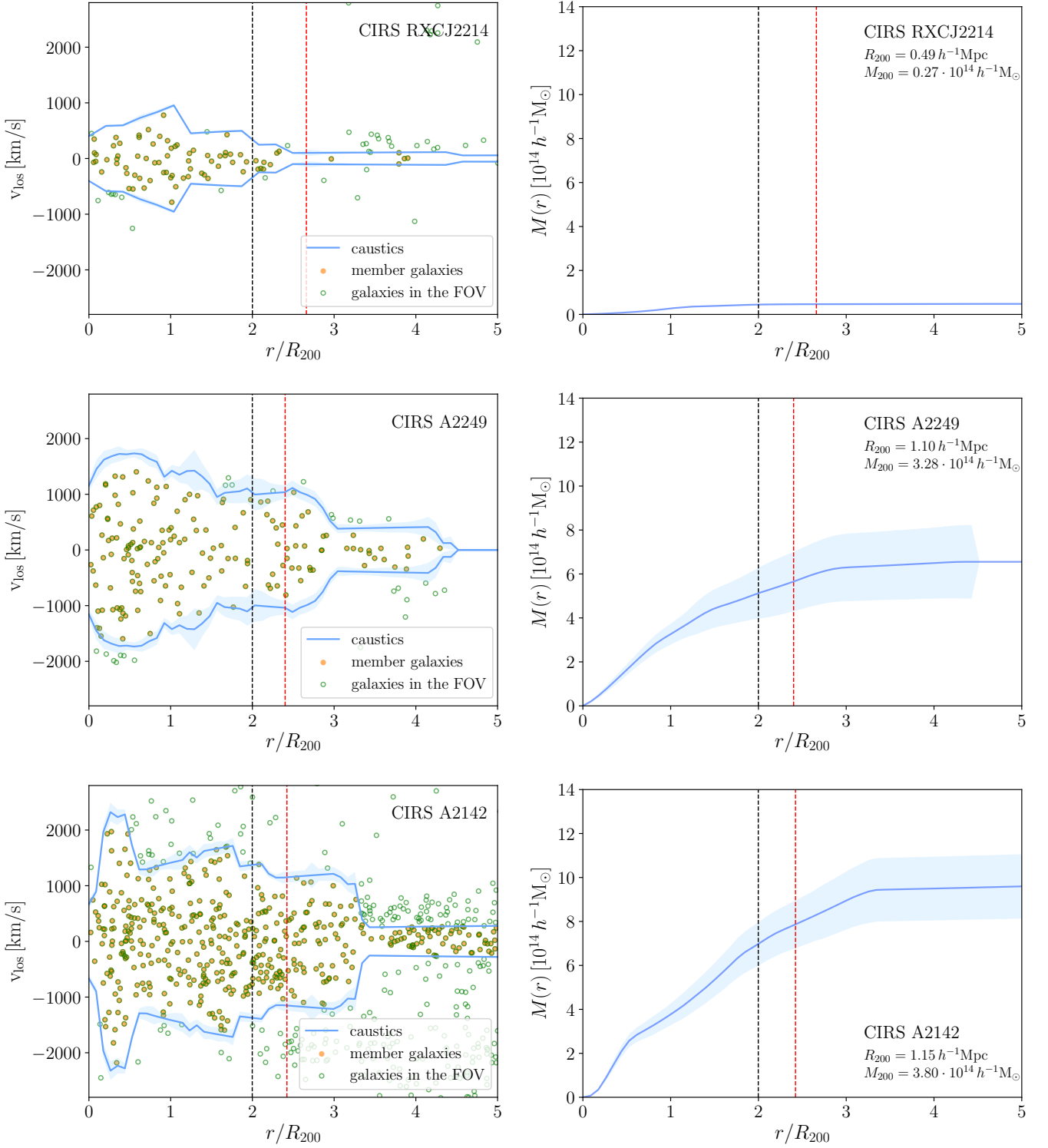


**Fig. 11.** Three examples of the estimation of the MAR for individual clusters in CIRS. The left and right columns show the R-v diagram (left) and mass profile (right) for each cluster. The black and red dashed lines show the inner and outer radius of the infalling spherical shell. The mass of the shell used to estimate the MAR is in the legend. The  $M_{200}$  of the clusters increases from top to bottom.

The error bars show the 68% percentile ranges of the distributions of the MAR and of the redshift of the clusters.

To compare these measured MARs with the expectations of the  $\Lambda$ CDM model, Fig. 14 shows the results of Fig. 4 for the simulated clusters extracted from the L-CoDECS simulation (Sect. 3.2). The blue squares show the medians of the MARs derived

from the three-dimensional mass profiles. The red triangles show the medians of the MARs derived from the caustic mass profiles estimated from the mock redshift surveys.

This figure confirms the result of Fig. 13: the medians of the MARs of real clusters fall within the range of the MAR of simulated clusters. The three median masses of the real cluster

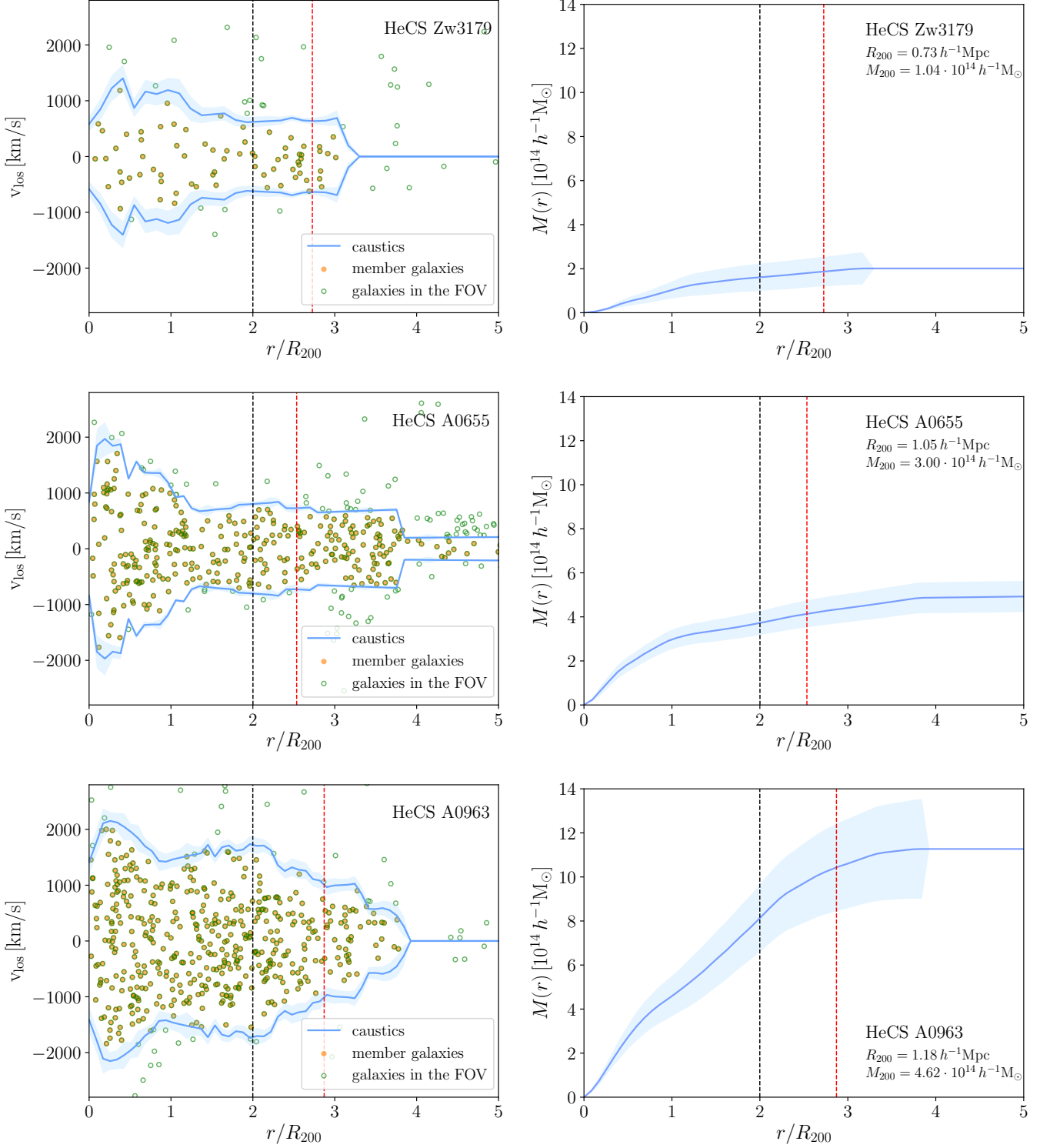


**Fig. 12.** Same as Fig. 11 for three HeCS clusters. Zw3179 and A655 belong to the low-mass sample, whereas A963 is in the high-mass sample.

samples,  $1.1$ ,  $2.2$ , and  $5.2 \times 10^{14} h^{-1} M_{\odot}$ , are in between the two median masses,  $10^{14}$  and  $10^{15} h^{-1} M_{\odot}$ , of the two samples of the simulated clusters.

Figure 14 also shows that the spreads in the median MARs of the real clusters are comparable with or even smaller than for the mock catalogues. This result supports the conclusion that the caustic technique returns robust estimates of the average MAR of clusters and that mock catalogues tend to overestimate the

expected uncertainties, because in the simulations the caustics are usually less well-defined than in the data (Sect. 3.4).

We now quantify the effect of the value of the initial velocity  $v_i$  on the estimate of the MAR. The empty circles in Fig. 14 show the median MARs of each cluster sample when we decrease  $v_i$  by 20 or 40% (cyan and blue circles) or increase  $v_i$  by 20 or 40% (orange and red circles) with respect to the adopted  $v_i$  (green dots with error bars). The estimated MAR does indeed depend on  $v_i$ ,

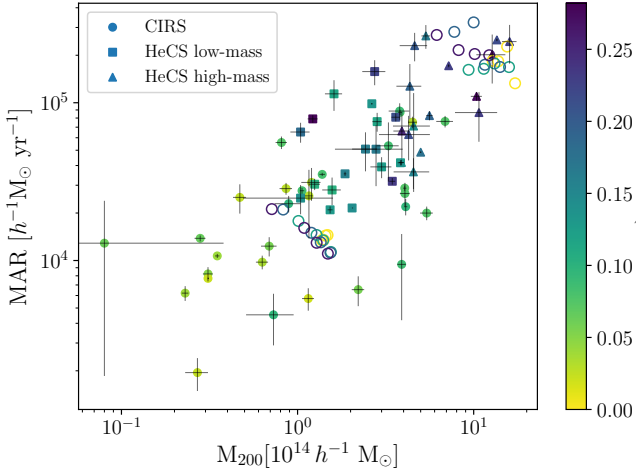


**Fig. 13.** MAR of individual clusters as a function of their  $M_{200}$ ; the colour code shows the dependence on redshift. Filled circles, squares and triangles refer to the CIRS, low- and high-mass HeCS sample, respectively. The empty circles show the median MARs of the  $N$ -body clusters of our two simulated samples; for these clusters, we estimate the MAR from their three-dimensional mass profiles.

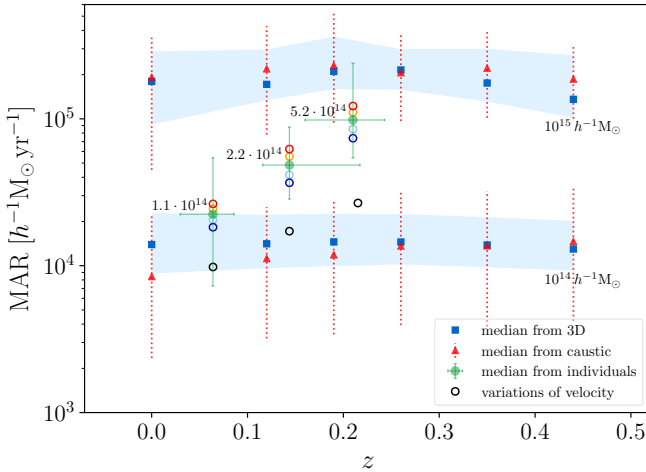


**Fig. 14.** Median MARs of real (green) and simulated (blue and red) clusters. The green error bars show the 68% percentile ranges of the MAR and redshift distributions of the real clusters. The value close to each green filled circle is the median mass  $M_{200}$  of the real clusters in units of  $h^{-1} M_{\odot}$ . The blue squares and red triangles are for the MAR based on the three-dimensional and the caustic mass profiles of simulated clusters, respectively (from Fig. 4). The light blue shaded areas and the red error bars are the 68% percentile range of the distribution of the individual MAR of the simulated clusters. The empty circles show the median MARs of real clusters for different values of the infall velocity. We show results where we change the initial infall velocity we adopt by -40% (blue), -20% (cyan), +20% (orange) or +40% (red). The black circles show the MAR estimated with an initial infall velocity  $v_i = 0$ .

but the resulting MARs remain within the 68% percentile range of the MAR distribution. The extreme and unrealistic choice  $v_i = 0$  makes the estimated MAR (black circles) decrease substantially: the MAR then disagrees significantly with the  $\Lambda$ CDM expectations. Nevertheless, the correlations between the MAR, redshift, and cluster mass persist regardless of the choice of  $v_i$ .

A simple analysis explains qualitatively why the correlations between MAR, redshift, and cluster mass are so robust. Around each cluster, we consider the mass  $M_{2-2.5}$  of the shell with inner and outer radius  $2.0R_{200}$  and  $2.5R_{200}$ , respectively. This shell is comparable to the shell usually identified by the solution of Equation (1). Figure 15 shows  $M_{2-2.5}$  as a function of the cluster mass  $M_{200}$ . The colour and symbols are the same as in Fig. 13. The two figures are qualitatively similar and show, as expected, that the correlations we see for the MAR derived directly from the correlations between  $M_{2-2.5}$ ,  $M_{200}$ , and  $z$ .

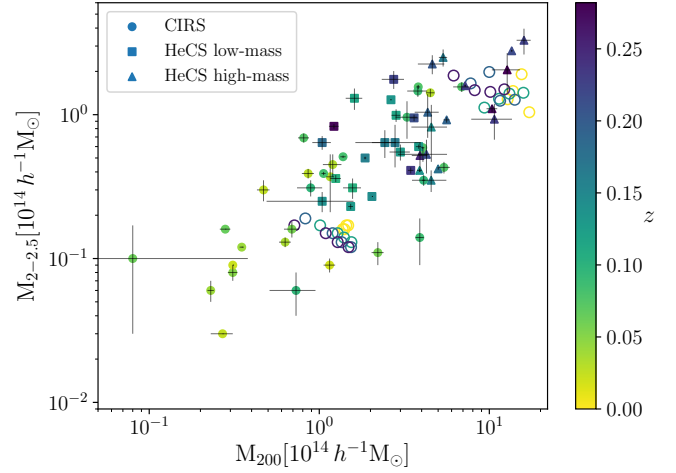


**Fig. 15.** Mass  $M_{2-2.5}$  of the shell with radii  $2.0R_{200}$  and  $2.5R_{200}$  as a function of  $M_{200}$ . The colour code shows the dependence on redshift. Circles, squares and triangles refer to the CIRS, low- and high-mass HeCS sample, respectively. The empty circles show the median  $M_{2-2.5}$  of the  $N$ -body clusters of our two simulated samples, estimated from their three-dimensional mass profiles.

A different strategy for estimating the mean MAR of real clusters is to apply our recipe to an average cluster obtained by stacking the real clusters (Rines & Diaferio 2006; Serra et al. 2011). This approach has the advantage of considering all the clusters of each sample, including those clusters where the individual MAR cannot be estimated. In addition, stacking the clusters averages out the deviations from spherical symmetry of the individual clusters.

Similarly to HeCS, we separate the CIRS sample into a low-mass and a high-mass subsample, according to the cluster median mass  $M_{200} = 1.78 \times 10^{14} h^{-1} M_{\odot}$ . Table 6 lists the median masses and the 68% percentile ranges of the mass and redshift distributions of the four subsamples. For each cluster subsample, we build a R-v diagram containing all the galaxies in the field of view with line-of-sight velocity within  $4000 \text{ km s}^{-1}$  from the cluster velocity and within  $10 h^{-1} \text{ Mpc}$  from the cluster centre. The “total” column of Table 7 shows the number of galaxies inside these four stacked clusters. In the R-v diagram of the stacked cluster, the velocities and the radial distances are expressed in the reference frame of each cluster without any additional normalization. This simple approach is justified by the homogeneity of mass and size for clusters within each subsample. The stacking procedure avoids introducing errors in the size and velocity dispersion of the clusters. If we stacked clusters of widely different mass we would require an additional normalization. The first and third panels of Figs. 17 and 18 show the R-v diagrams of the stacked clusters.

**Table 6.** CIRS AND HECS SUBSAMPLES FOR THE STACKED CLUSTERS

cluster sample	median $z$	68 <sup>th</sup> percentile range [redshift $z$ ]	median $M_{200}$ [ $10^{14}h^{-1}M_{\odot}$ ]	68 <sup>th</sup> percentile range [ $10^{14}h^{-1}M_{\odot}$ ]	$M_{200}^{stk}$ [ $10^{14}h^{-1}M_{\odot}$ ]
CIRS-STK1	0.055	0.025-0.083	0.88	0.31-1.2	$1.07 \pm 0.43$
CIRS-STK2	0.076	0.052-0.087	3.3	2.2-4.4	$3.3 \pm 1.1$
HeCS-STK1	0.14	0.12-0.18	1.9	1.0-2.9	$2.8 \pm 0.57$
HeCS-STK2	0.20	0.14-0.25	5.6	4.4-11.8	$7.3 \pm 1.8$

**Table 7.** GALAXIES INSIDE THE STACKED CLUSTERS

cluster sample	total	members-only	equally-weighted
CIRS-STK1	17361	5243	7151
CIRS-STK2	26868	12161	15615
HeCS-STK1	11686	5300	6589
HeCS-STK2	12745	7982	6456

The mass profiles estimated with the caustic technique applied to these R-v diagrams are shown in the second and fourth panels of Figs. 17 and 18. The masses  $M_{200}$  of the stacked clusters are listed in Table 6 with their uncertainty.

To estimate the MAR, we need to set the value of the initial infall velocity  $v_i$ . With the same procedure described in Sect. 5.1, we use the L-CoDECS simulations to find  $v_i = -154 \pm 3 \text{ km s}^{-1}$ , and  $v_i = -302 \pm 11 \text{ km s}^{-1}$  for the low- and high-mass CIRS subsample, and  $v_i = -282 \pm 7 \text{ km s}^{-1}$  and  $v_i = -757 \pm 28 \text{ km s}^{-1}$ , for the low- and high-mass HeCS subsample, respectively.

Figures 17 and 18 show the inner (black dashed line) and outer radius (red dashed line) of the infalling shell, according to Equation (1). Averaging out the deviations from spherical symmetry and increasing the number of member galaxies make the caustic location and the mass profiles appear smoother than those of individual clusters (e.g., Figs. 11 and 12).

Figure 16 shows the MAR of the stacked clusters (orange circles), superimposed on the results obtained from individual clusters (Fig. 14, green circles). The MARs of the stacked clusters are consistent with the median MARs of the individual clusters thus confirming the dependence of the MAR on cluster mass and redshift and reflecting the predictions of the  $\Lambda$ CDM model.

The uncertainty in the MARs of the stacked clusters are also consistent with the spread of the distributions of the individual MARs. The relative uncertainty in the MARs of the stacked clusters are  $\sim 64\%$ , larger than the relative uncertainties in the individual MARs ( $\leq 17\%$ ). Although the stacked clusters more closely satisfy the assumption of spherical symmetry, the increase of the number of background and foreground galaxies in the R-v diagram makes the location of the caustics more uncertain and, consequently, increases the uncertainty on the mass profile.<sup>4</sup> Nevertheless, as expected, most members of the stacked clusters are members of the individual clusters: 75%, 81%, 80%

and 94% of the members of CIRS-STK1, CIRS-STK2, HeCS-STK1 and HeCS-STK2, respectively, are members of the individual clusters. Hence, the location of the caustic curves appears to be robust.

We can reduce the uncertainty on the mass profile by adopting a different strategy to build the stacked clusters. For each cluster, we now include only the member galaxies identified by the caustic technique, namely the galaxies within the caustics in each R-v diagram. Again, we include all the clusters, irrespective of the fact that their caustic amplitude can be zero beyond  $2R_{200}$ . The “members-only” column of Table 7 shows the number of galaxies inside these four stacked clusters. Clearly, the number of galaxies in the R-v diagrams substantially drops compared to the previous stacked clusters: for the two mass bins of CIRS, the number of galaxies is reduced by 70% and 55%, respectively; for the HeCS subsamples, these numbers decrease by 55% and 43%. The R-v diagrams of these new stacked clusters have now well-defined trumpets and the caustics identify substantially fewer interlopers. As expected, the mean relative uncertainty in the estimated MAR drops to  $\sim 36\%$ , approximately half of the relative uncertainty of the previous stacked clusters. Although the new MAR estimates are  $\sim 12\%$  smaller, on average, than the previous MAR’s, because the R-v diagrams are now slightly less sampled than the original stacked clusters, the difference between the two MAR estimates is within the uncertainties and the estimates are thus statistically consistent with each other.

In the stacking procedure, for each cluster, we include all the galaxies in the field of view within  $4000 \text{ km s}^{-1}$  along the line of sight and within  $10h^{-1} \text{ Mpc}$  from the cluster centre without any further normalization of the line-of-sight velocity and projected distance of the cluster galaxies. The properties of the stacked cluster might thus mirror the properties of the clusters that contribute most galaxies and are presumably more massive. To quantify this effect, we now create new stacked clusters. For each cluster, we include the same number  $N$  of galaxies randomly sampled from the field of view: for each mass bin, we set  $N$  close to the number of galaxies of the cluster with the smallest number of galaxies. For the two mass bins of CIRS, we have  $N = 263$  and  $N = 571$ ; for HeCS, we have  $N = 402$  and  $N = 408$ . These values of  $N$  preserve the optimal number of galaxies  $\geq 200$  within  $3R_{200}$  (Serra et al. 2011). Only 5 out of 36 clusters in the low-mass subsample of CIRS have fewer galaxies than  $N = 263$ ; the clusters with fewer galaxies than  $N$  are 2 out of 35, 1 out of 26, and 2 out of 26 for the high-mass subsample of CIRS, and for the low- and high-mass subsamples of HeCS, respectively. The “equally-weighted” column of Table 7 shows the number of galaxies inside these four stacked clusters. These equally-weighted stacked clusters have a R-v diagram slightly less sampled than the original stacked clusters.

certainty on the mass increases (Equation 5). For example CIRS-STK2 has  $\varepsilon \sim 0.35$ , and a relative error in the MAR of  $\sim 70\%$ .

<sup>4</sup> The number density of background and foreground galaxies in the R-v diagram affects the estimate of the uncertainties in the mass profile. The relative uncertainty in the caustic amplitude is  $\varepsilon = \sigma_{\mathcal{A}}/\mathcal{A} = \kappa/\max\{f(r, v_{\text{los}})\}$ , where  $f(r, v_{\text{los}})$  is the galaxy number density in the R-v diagram and  $\kappa$  is the threshold identified by the algorithm to locate the caustics. Larger number densities of background and foreground galaxies tend to decrease  $\max\{f(r, v_{\text{los}})\}$ ;  $\varepsilon$  thus increases and, in turn, the un-

As a consequence, their MAR's are, on average, 9% lower than the previous MAR's, and their relative uncertainties are, on average,  $\sim 25\%$  larger. Nevertheless, their MAR's estimates are still consistent with the results of Fig. 16.

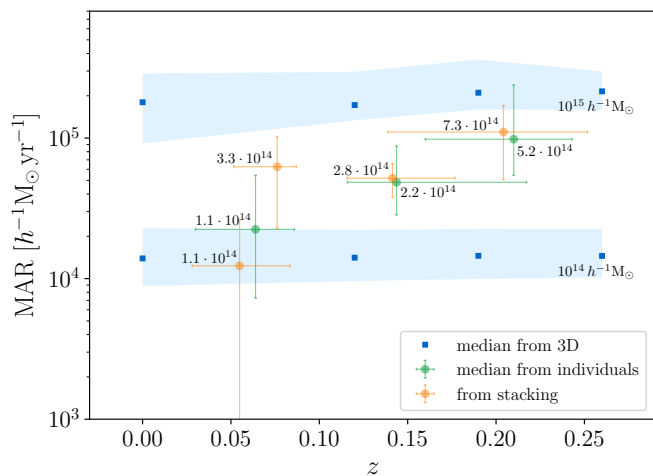


**Fig. 16.** MARs of the stacked clusters of CIRS (the two orange circles at low redshift) and HeCS (the two orange circles at high redshift). The median MARs of the individual clusters from Fig. 14 are shown in green. The value close to each circle is the mass  $M_{200}$  in units of  $h^{-1} M_{\odot}$ . The blue squares with the shaded bands are from Fig. 4 and show the median MARs and their spreads of the simulated clusters estimated with the three-dimensional mass profiles.

## 6. Discussion

Our result is the first attempt to measure the MAR of clusters of galaxies by estimating the amount of mass in the outer regions. Our approach is crucially different from the approach usually adopted in the theoretical investigations of the accretion of dark matter halos. Most attention is focused on the connection between the accretion history of halos, and their global properties at a particular epoch (e.g., Rey et al. 2019). These properties include the concentration parameter of the NFW profile (Navarro et al. 1997) and the amount of substructure (Jing 2000). More recently, Ludlow et al. (2013) show that the ubiquity of the NFW density profile in CDM models results from the mass independence of the accretion histories of dark matter halos.

The accretion histories of dark matter halos can in principle be a very sensitive probe of the nature of the dark matter particles and of the theory of gravity. For example, both self-interacting dark matter particles (Brinckmann et al. 2018) and warm dark matter particles (Ludlow et al. 2016) predict smaller concentrations for similar halo masses, which on turn affect the determination of the formation redshift of the dark matter halos. On the other hand, Oleśkiewicz et al. (2019) show that in the Hu & Sawicki (2007) form of  $f(R)$  gravity, the linear relation between concentration and formation time, seen in CDM models, becomes more complicated due to gravitational screening.

Unfortunately, when moving from dark matter halos to real cluster of galaxies, the differences detected in the theoretical relations might appear out of reach, because the formation redshift is an unobservable quantity and the concentration parameter is prone to various systematic errors and sample biases (Mandelbaum et al. 2008; Bartelmann 2010; Oguri et al. 2012). Moreover, the properties of the central region of clusters, say at

$\lesssim 0.1R_{200}$ , are complicated by the physics of baryons, as they can play a relevant role in the dynamics of the cluster centre (Blumenthal et al. 1986; Kravtsov et al. 2005).

$N$ -body simulations suggest that the mass that is falling onto the cluster for the first time is located beyond the splash-back radius  $\sim 2R_{200}$  (Diemer & Kravtsov 2014; More et al. 2015). However, to date most investigations of the accretion rate of real clusters focus on regions inside this radius (e.g. Lemze et al. 2013; Haines et al. 2018). Therefore, comparing their results with the MAR derived from  $N$ -body simulations is not obvious.

On the contrary, the estimation of the mass at distances  $\gtrsim 2R_{200}$  is a more straightforward approach, because this mass is falling onto the cluster for the first time and is thus a direct estimate of the accretion rate. In addition, in this region baryons should have a limited effect because gravity is the main driver of the properties of the density and velocity fields. Estimating the mass in these outer regions is inaccessible to X-ray and strong lensing measurements, but can be tackled with the caustic technique or weak gravitational lensing. Thanks to the caustic technique, estimating the mass at these large radii, where dynamical equilibrium does not hold, becomes feasible when appropriately dense spectroscopic surveys are available.

Nevertheless, the technique we present has two potential observational limitations: the use of  $N$ -body simulations for setting the value of the infall velocity, and the removal of the real clusters with a sparse spectroscopic sampling when computing the individual MAR. At present, the former issue cannot be solved, because the measurement of the radial velocity of cluster galaxies is not currently feasible. We can in principle remove the necessity of including the infall velocity from  $N$ -body simulations, as well as the assumption of the infall time, by adopting the mass within the shell  $[2, 2.5]R_{200}$  as an appropriate prior of the MAR, as Figs. 15 and 13 suggest.

The issue of removing clusters from the samples of clusters with individual MAR concerns the distribution of the galaxies within the R-v diagram. The caustics of  $\sim 65\%$  of the removed clusters have unphysical spikes that lead the caustic technique to refrain from estimating the mass at large radii. Usually, a spike emerges when there is an asymmetric lack of galaxies with respect to the line  $v_{\text{los}} = v_{\text{cl}}$  in the R-v diagram. This lack of galaxies can originate either from a poor spectroscopic sampling or from a real underdense region around the cluster: clusters are generally not spherically symmetric, as assumed by the caustic technique, and asymmetric galaxy distributions on the sky can generate inhomogeneous galaxy distributions in the R-v diagrams. For clusters with a spike resulting from poor sampling rather than an actual underdense region, we estimate that the caustic technique could properly locate the caustics if the spectroscopic sampling were increased by  $\sim 15\%$  in a stripe, of the R-v diagram, of thickness  $\sim 0.5 h^{-1} \text{ Mpc}$  centered on the spike. In principle, we could thus be able to recover  $\sim 55\%$  of the clusters removed in both CIRS and HeCS. The remaining clusters either (i) are less massive and thus have a poorly populated R-v diagram or (ii) are embedded in a particularly dense region and the caustic algorithm is unable, at large radii, to properly distinguish between galaxy members and interlopers and locate the caustics.

The growth of cosmic structures on linear scales can be different in different dark energy models and modified gravity models (e.g., Burrage et al. 2017; Giocoli et al. 2018; Perenon et al. 2019). In principle, the MAR, that measures the growth on non-linear scales, can be a tool to discriminate among different theories, similarly to the cluster mass function (Kopp et al. 2013; Lombriser et al. 2013; Cataneo et al. 2016; Barreira et al. 2013).



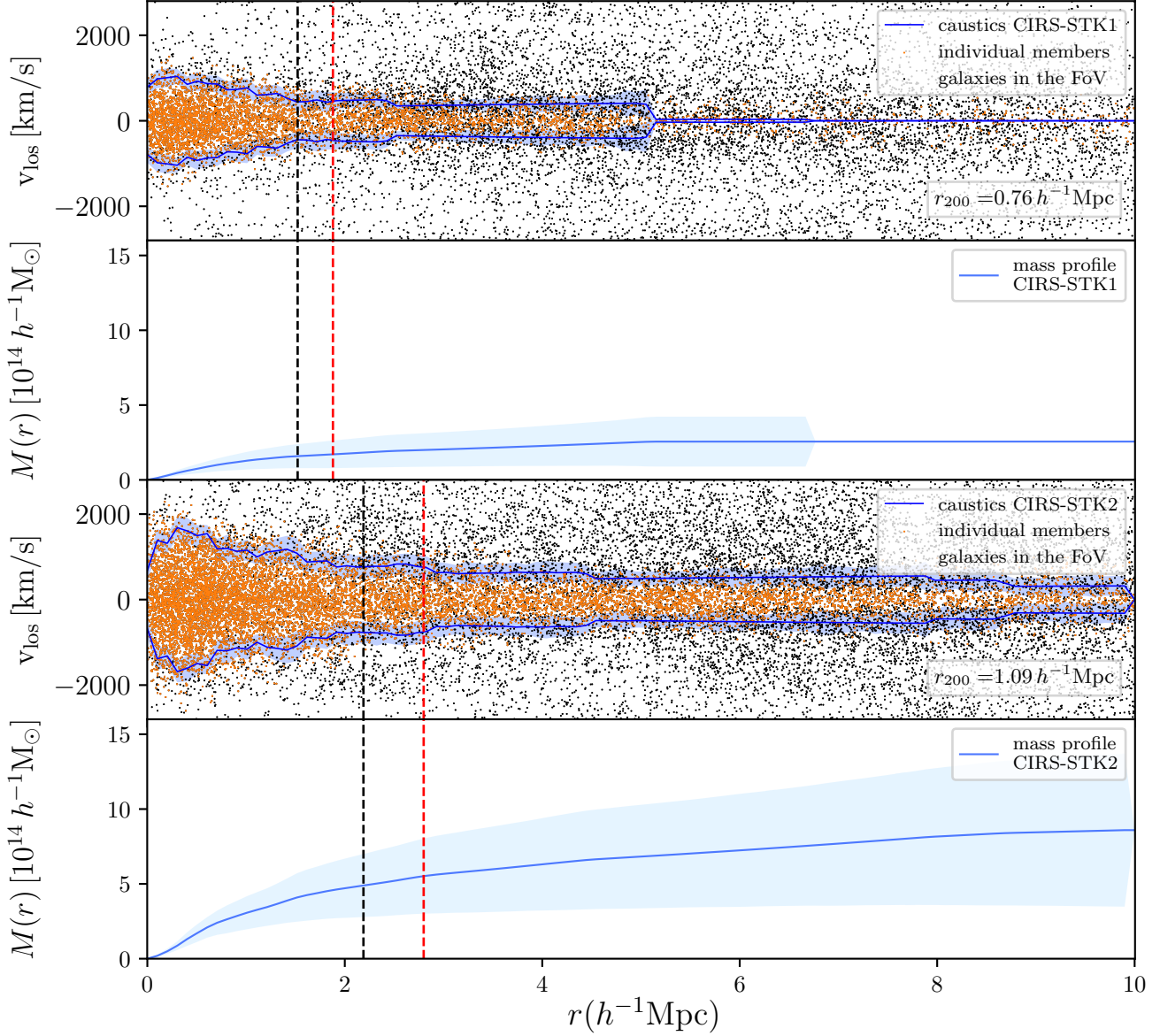


**Fig. 17.** R-v diagrams and corresponding mass profiles of the two stacked clusters from the CIRS catalogue. The upper (lower) panels refer to low-mass (high-mass) subsample. The black and red dashed vertical lines show the inner and outer radius of the spherical shell used to estimate the MAR. The shaded areas show the 50% confidence level of the caustic location and of the caustic mass profile according to the caustic technique recipe.

However, the sensitivity of the MAR on the theory of gravity remains to be investigated in detail (e.g., Zentner 2007). Similarly, it remains to be seen whether the MAR estimated with the caustic method for clusters at different redshift and with different mass are accurate enough to distinguish among the models. Specifically, we need to assess the optimal balance between the number of observed clusters and their spectroscopy sampling, required to reach the necessary sensitivity. However, estimating the mass in the cluster outer regions might not even be necessary to probe the theory of gravity, but the velocity field can suffice. For example, in his cosmological  $N$ -body simulations in the MOND framework, Candlish (2016) shows that the velocity field in the

outskirts of clusters is significantly enhanced compared to standard gravity. We plan to tackle these issues in future work.

## 7. Conclusion

We use the dense redshift surveys of the CIRS (Rines & Diaferio 2006) and HeCS (Rines et al. 2013) clusters to make the first measurement of the MAR of 129 clusters in the redshift range  $0.01 < z < 0.3$  and in the mass range  $10^{14} - 10^{15} h^{-1} M_{\odot}$ .

Our measurement is based on the spherical accretion recipe suggested by De Boni et al. (2016), where the MAR is estimated from the mass of a shell, of appropriate thickness, surrounding

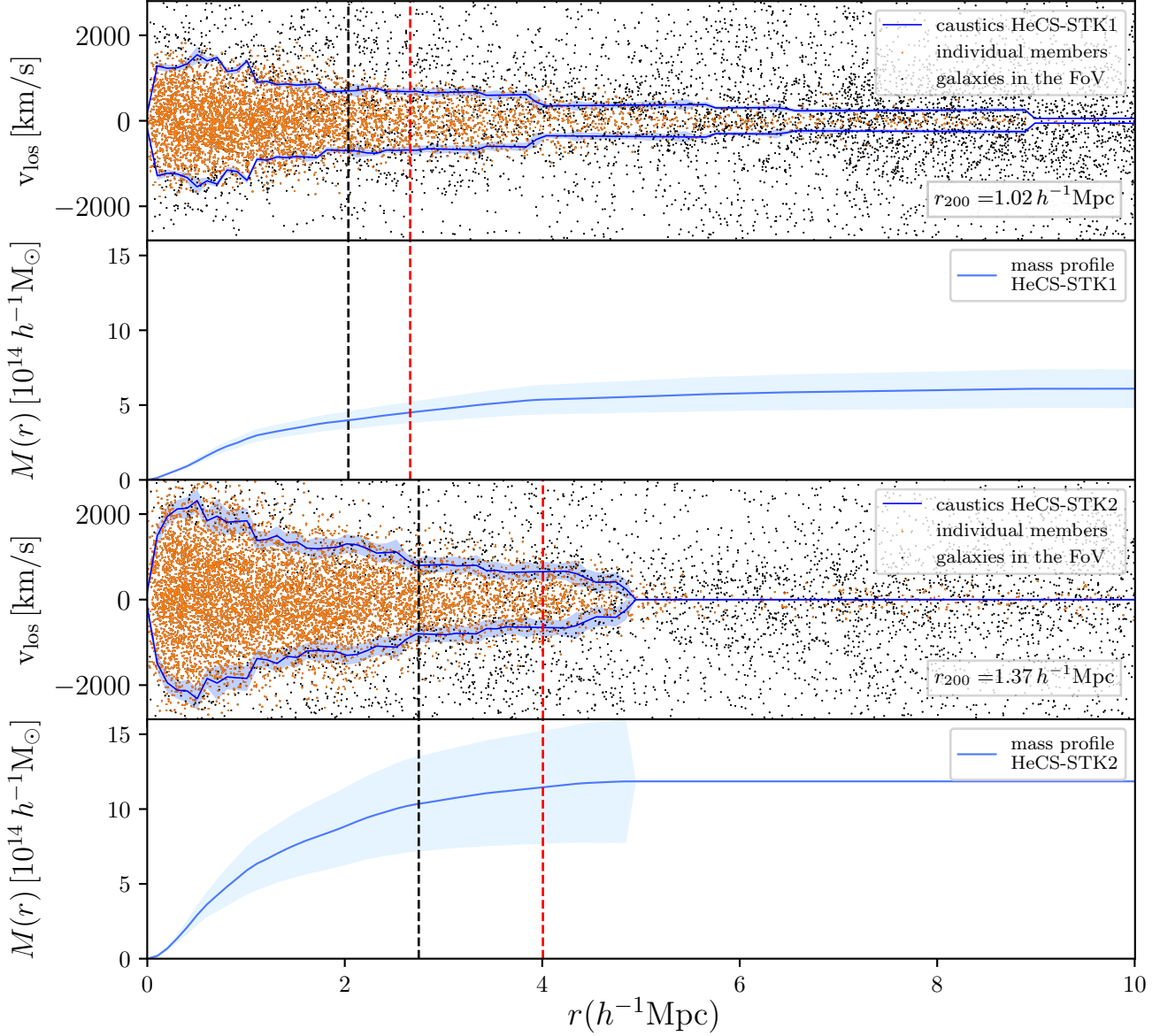


**Fig. 18.** Same as Fig. 17 for the HeCS catalogue.

the cluster. We set the inner radius of the shell at  $2R_{200}$ . The shell thickness is typically  $\sim 0.5R_{200}$ . To estimate the shell mass at these large radii, we use the caustic technique. When applied to mock redshift surveys of simulated clusters in the same range of redshift and mass, our procedure returns an unbiased MAR within  $\sim 17\%$  of the true MAR, on average.

Our estimates of the MARs of the CIRS and HeCS clusters agree with the MARs of the dark matter halos extracted from a  $\Lambda$ CDM N-body model (Baldi 2012), in the same mass and redshift range. As in the simulations, the observed cluster MARs increase with cluster mass and redshift.

The observed correlations of the MAR with cluster mass and redshift are shared by the mass of the infalling shell. We thus suggest that the mass of the shell can be a proxy of the MAR.

The MAR estimates for individual clusters have typical uncertainties of 17%; for the stacked MARs the uncertainty is  $\sim 36\%$ . Systematic errors resulting from sample selection could impact these results. We show that neither CIRS nor HeCS have significant photometric incompleteness as a function of radius. However, HeCS misses at most  $\sim 30\%$  of the blue galaxies compared to CIRS; the spectroscopic completeness of both CIRS and HeCS drops to  $\sim 50\%$  at radii larger than  $\sim 2R_{200}$ . Nevertheless, neither the photometric nor the spectroscopic incompleteness biases the MAR estimates. The systematics are within the random errors of the caustic technique.

Measurement of the MAR holds promise for more stringent tests of the standard  $\Lambda$ CDM paradigm. With much larger cluster samples it may also distinguish between different models of dark matter and of modified gravity. These tests require dense, com-



plete spectroscopic surveys that extend to large cluster-centric radius.

Extension of the cluster survey to significantly higher redshift provides a broader baseline for these tests. For example, N-body simulations predict that the accretion rate at  $z = 0.7$  is  $\sim 2.6$  times larger than at the current epoch (McBride et al. 2009). To this redshift both the caustic technique and the weak lensing method can readily be applied. Deep photometric surveys along with the multi-object spectrographs like the Prime Focus Spectrograph on Subaru (Takada et al. 2014) will enable this extension on the observational side. Advances in simulations (Giocoli et al. 2018) will be important for refining the model tests.

**Acknowledgements.** An early version of this work was the Master thesis in Physics at the University of Torino of SDG. CDB thanks Benedikt Diemer for useful discussion on the splashback radius. The graduate-student fellowship of MP is supported by the Italian Ministry of Education, University and Research (MIUR) under the *Departments of Excellence* grant L.232/2016. We also acknowledge partial support from the INFN grant InDark. This research has made use of NASA's Astrophysics Data System Bibliographic Services.

## References

- Achitouv, I., Wagner, C., Weller, J., & Rasera, Y. 2014, *J. Cosmology Astropart. Phys.*, 2014, 077
- Ade, P., Aghanim, N., Arnaud, M., et al. 2016, *Astronomy & Astrophysics*, 594, A27
- Adelman-McCarthy, J. K., Agüeros, M. A., Allam, S. S., et al. 2008, *ApJS*, 175, 297
- Adelman-McCarthy, J. K., Agüeros, M. A., Allam, S. S., et al. 2006, *The Astrophysical Journal Supplement Series*, 162, 38
- Adhikari, S., Dalal, N., & Chamberlain, R. T. 2014, *JCAP*, 11, 019
- Allgood, B., Flores, R. A., Primack, J. R., et al. 2006, *Monthly Notices of the Royal Astronomical Society*, 367, 1781
- Armitage, T. J., Barnes, D. J., Kay, S. T., et al. 2018, *MNRAS*, 474, 3746
- Baldi, M. 2012, *MNRAS*, 422, 1028
- Bardeen, J. M., Szalay, A., Kaiser, N., & Bond, J. 1985, *Astrophys. J.*, 304, 15
- Barreira, A., Li, B., Baugh, C. M., & Pascoli, S. 2013, *Journal of Cosmology and Astroparticle Physics*, 2013, 056
- Bartelmann, M. 2010, *Classical and Quantum Gravity*, 27, 233001
- Baxter, E., Chang, C., Jain, B., et al. 2017, *ApJ*, 841, 18
- Bett, P., Eke, V., Frenk, C. S., et al. 2007, *Monthly Notices of the Royal Astronomical Society*, 376, 215
- Blumenthal, G. R., Faber, S. M., Flores, R., & Primack, J. R. 1986, *ApJ*, 301, 27
- Bower, R. G. 1991, *Monthly Notices of the Royal Astronomical Society*, 248, 332
- Brinckmann, T., Zavala, J., Rapetti, D., Hansen, S. H., & Vogelsberger, M. 2018, *MNRAS*, 474, 746
- Burrage, C., Parkinson, D., & Seery, D. 2017, *Physical Review D*, 96, 043509
- Busch, P. & White, S. D. M. 2017, *MNRAS*, 470, 4767
- Candlish, G. N. 2016, *MNRAS*, 460, 2571
- Casagrande, L. & Diaferio, A. 2006, *Monthly Notices of the Royal Astronomical Society*, 373, 179
- Cataneo, M., Rapetti, D., Lombriser, L., & Li, B. 2016, *Astropart. Phys.*, 12, 1607
- Chang, C., Baxter, E., Jain, B., et al. 2018, *The Astrophysical Journal*, 864, 83
- Contigiani, O., Hoekstra, H., & Bahé, Y. M. 2019, *MNRAS*, 485, 408
- Corasaniti, P. S. & Achitouv, I. 2011, *Phys. Rev. Lett.*, 106, 241302
- Correa, C. A., Wyithe, J. S. B., Schaye, J., & Duffy, A. R. 2015, *MNRAS*, 450, 1514
- De Boni, C., Serra, A. L., Diaferio, A., Giocoli, C., & Baldi, M. 2016, *ApJ*, 818, 188
- de Haan, T., Benson, B. A., Bleem, L. E., et al. 2016, *ApJ*, 832, 95
- De Simone, A., Maggiore, M., & Riotto, A. 2011, *Monthly Notices of the Royal Astronomical Society*, 418, 2403
- Diaferio, A. 1999, *MNRAS*, 309, 610
- Diaferio, A. & Geller, M. J. 1997, *ApJ*, 481, 633
- Diaferio, A., Geller, M. J., & Rines, K. J. 2005, *The Astrophysical Journal Letters*, 628, L97
- Diemand, J., Moore, B., & Stadel, J. 2004, *Monthly Notices of the Royal Astronomical Society*, 352, 535
- Diemer, B. & Kravtsov, A. V. 2014, *ApJ*, 789, 1
- Fabricant, D., Fata, R., Roll, J., et al. 2005, *PASP*, 117, 1411
- Fakhouri, O., Ma, C.-P., & Boylan-Kolchin, M. 2010, *MNRAS*, 406, 2267
- Gao, L., White, S. D. M., Jenkins, A., Stoehr, F., & Springel, V. 2004, *Monthly Notices of the Royal Astronomical Society*, 355, 819
- Geller, M. J., Diaferio, A., & Kurtz, M. J. 1999, *The Astrophysical Journal*, 517, L23
- Geller, M. J., Diaferio, A., & Kurtz, M. J. 2011, *AJ*, 142, 133
- Geller, M. J., Diaferio, A., Rines, K. J., & Serra, A. L. 2013, *The Astrophysical Journal*, 764, 58
- Genel, S., Genzel, R., Bouché, N., et al. 2008, *The Astrophysical Journal*, 688, 789
- Giocoli, C., Baldi, M., & Moscardini, L. 2018, *Monthly Notices of the Royal Astronomical Society*, 481, 2813
- Giocoli, C., Tormen, G., & Sheth, R. K. 2012, *Monthly Notices of the Royal Astronomical Society*, 422, 185
- Haines, C. P., Finoguenov, A., Smith, G. P., et al. 2018, *MNRAS*, 477, 4931
- Hellwing, W. A., Schaller, M., Frenk, C. S., et al. 2016, *MNRAS*, 461, L11
- Hoekstra, H. 2003, *MNRAS*, 339, 1155
- Hoekstra, H., Hartlap, J., Hilbert, S., & van Uitert, E. 2011, *MNRAS*, 412, 2095
- Hu, W. & Sawicki, I. 2007, *Phys. Rev. D*, 76, 064004
- Hurier, G. 2019, arXiv preprint arXiv:1904.06951
- Hwang, H. S., Geller, M. J., Diaferio, A., Rines, K. J., & Zahid, H. J. 2014, *ApJ*, 797, 106
- Jarrett, T. 2004, *Publications of the Astronomical Society of Australia*, 21, 396–403
- Jiang, F. & van den Bosch, F. C. 2014, *Monthly Notices of the Royal Astronomical Society*, 440, 193
- Jing, Y. P. 2000, *ApJ*, 535, 30
- Kasun, S. & Evrard, A. E. 2005, *The Astrophysical Journal*, 629, 781
- Kauffmann, G., White, S. D. M., & Guiderdoni, B. 1993, *Monthly Notices of the Royal Astronomical Society*, 264, 201
- Komatsu, E., Smith, K. M., Dunkley, J., et al. 2011, *ApJS*, 192, 18
- Kopp, M., Appleby, S. A., Achitouv, I., & Weller, J. 2013, *Physical Review D*, 88, 084015
- Kravtsov, A. V., Nagai, D., & Vikhlinin, A. A. 2005, *The Astrophysical Journal*, 625, 588
- Kuhlen, M., Vogelsberger, M., & Angulo, R. 2012, *Physics of the Dark Universe*, 1, 50, next Decade in Dark Matter and Dark Energy
- Lacey, C. & Cole, S. 1993, *Monthly Notices of the Royal Astronomical Society*, 262, 627
- Lemze, D., Postman, M., Genel, S., et al. 2013, *The Astrophysical Journal*, 776, 91
- Lombriser, L., Li, B., Koyama, K., & Zhao, G.-B. 2013, *Physical review D*, 87, 123511
- Ludlow, A. D., Bose, S., Angulo, R. E., et al. 2016, *Monthly Notices of the Royal Astronomical Society*, 460, 1214
- Ludlow, A. D., Navarro, J. F., Boylan-Kolchin, M., et al. 2013, *MNRAS*, 432, 1103
- Mandelbaum, R., Seljak, U., & Hirata, C. M. 2008, *Journal of Cosmology and Astroparticle Physics*, 2008, 006
- McBride, J., Fakhouri, O., & Ma, C.-P. 2009, *MNRAS*, 398, 1858
- More, S., Diemer, B., & Kravtsov, A. V. 2015, *ApJ*, 810, 36
- More, S., Diemer, B., & Kravtsov, A. V. 2015, *The Astrophysical Journal*, 810, 36
- More, S., Miyatake, H., Takada, M., et al. 2016, *ApJ*, 825, 39
- Musso, M., Cadiou, C., Pichon, C., et al. 2018, *MNRAS*, 476, 4877
- Navarro, J. F., Frenk, C. S., & White, S. D. M. 1997, *ApJ*, 490, 493
- Oguri, M., Bayliss, M. B., Dahle, H., et al. 2012, *Monthly Notices of the Royal Astronomical Society*, 420, 3213
- Oleśkiewicz, P., Baugh, C. M., & Ludlow, A. D. 2019, *MNRAS*, 489, 4658
- Parkinson, H., Cole, S., & Helly, J. 2007, *Monthly Notices of the Royal Astronomical Society*, 383, 557
- Perenon, L., Bel, J., Maartens, R., & de La Cruz-Dombriz, A. 2019, *Journal of Cosmology and Astroparticle Physics*, 2019, 020
- Planck Collaboration, Aghanim, N., Akrami, Y., et al. 2018, arXiv e-prints, arXiv:1807.06209
- Power, C., Knebe, A., & Knollmann, S. R. 2011, *Monthly Notices of the Royal Astronomical Society*, 419, 1576
- Press, W. H. & Schechter, P. 1974, *The Astrophysical Journal*, 187, 425
- Ragone-Figueroa, C., Plionis, M., Merchán, M., Gottlöber, S., & Yepes, G. 2010, *Monthly Notices of the Royal Astronomical Society*, 407, 581
- Ragozzine, B., Clowe, D., Markevitch, M., Gonzalez, A. H., & Bradač, M. 2011, *The Astrophysical Journal*, 744, 94
- Rey, M. P., Pontzen, A., & Saintonge, A. 2019, *MNRAS*, 485, 1906
- Rines, K. & Diaferio, A. 2006, *AJ*, 132, 1275
- Rines, K., Geller, M. J., Diaferio, A., & Kurtz, M. J. 2013, *ApJ*, 767, 15
- Rines, K., Geller, M. J., Kurtz, M. J., & Diaferio, A. 2003, *AJ*, 126, 2152
- Rines, K., Mahdavi, A., Geller, M. J., et al. 2001, *The Astrophysical Journal*, 555, 558
- Rines, K. J., Geller, M. J., Diaferio, A., Hwang, H. S., & Sohn, J. 2018, *ApJ*, 862, 172
- Schmalzing, J. & Diaferio, A. 2000, *MNRAS*, 312, 638

- Serra, A. L. & Diaferio, A. 2013, *ApJ*, 768, 116
- Serra, A. L., Diaferio, A., Murante, G., & Borgani, S. 2011, *MNRAS*, 412, 800
- Sheth, R. K. & Tormen, G. 2002, *Monthly Notices of the Royal Astronomical Society*, 329, 61
- Shin, T., Adhikari, S., Baxter, E. J., et al. 2019, *MNRAS*, 487, 2900
- Sohn, J., Geller, M. J., Diaferio, A., & Rines, K. J. 2019b, *Velocity Dispersions of Brightest Cluster Galaxies and Their Host Clusters*
- Sohn, J., Geller, M. J., Rines, K. J., et al. 2018, *ApJ*, 856, 172
- Sohn, J., Geller, M. J., Walker, S. A., et al. 2019a, *ApJ*, 871, 129
- Sohn, J., Geller, M. J., Zahid, H. J., et al. 2017, *The Astrophysical Journal Supplement Series*, 229, 20
- Somerville, R. S. & Kolatt, T. S. 1999, *Monthly Notices of the Royal Astronomical Society*, 305, 1
- Springel, V., Yoshida, N., & White, S. D. M. 2001, *MNRAS*, 6, 79
- Stoughton, C., Lupton, R. H., Bernardi, M., et al. 2002, *AJ*, 123, 485
- Sunayama, T. & More, S. 2019, *MNRAS*, 490, 4945
- Takada, M., Ellis, R. S., Chiba, M., et al. 2014, *Publications of the Astronomical Society of Japan*, 66
- Tasitsiomi, A., Kravtsov, A. V., Gottlober, S., & Klypin, A. A. 2004, *The Astrophysical Journal*, 607, 125
- Tchernin, C., Eckert, D., Ettori, S., et al. 2016, *Astronomy & Astrophysics*, 595, A42
- Umetsu, K. & Diemer, B. 2017, *The Astrophysical Journal*, 836, 231
- van den Bosch, F. C. 2002, *Monthly Notices of the Royal Astronomical Society*, 331, 98
- van den Bosch, F. C., Jiang, F., Hearin, A., et al. 2014, *MNRAS*, 445, 1713
- Van Den Bosch, F. C., Tormen, G., & Giocoli, C. 2005, *Monthly Notices of the Royal Astronomical Society*, 359, 1029
- Vitvitska, M., Klypin, A. A., Kravtsov, A. V., et al. 2002, *The Astrophysical Journal*, 581, 799
- Voges, W., Aschenbach, B., Boller, T., et al. 1999, *A&A*, 349, 389
- Wechsler, R. H., Bullock, J. S., Primack, J. R., Kravtsov, A. V., & Dekel, A. 2002, *The Astrophysical Journal*, 568, 52
- White, S. D. M. & Rees, M. J. 1978, *Monthly Notices of the Royal Astronomical Society*, 183, 341
- Xhakaj, E., Diemer, B., Leauthaud, A., et al. 2019, *arXiv e-prints*, arXiv:1911.09295
- Zentner, A. R. 2007, *International Journal of Modern Physics D*, 16, 763
- Zhang, J., Ma, C.-P., & Fakhouri, O. 2008, *Monthly Notices of the Royal Astronomical Society: Letters*, 387, L13
- Zhao, D. H., Jing, Y. P., Mo, H. J., & Börner, G. 2009, *The Astrophysical Journal*, 707, 354
- Zubeldia, Í. & Challinor, A. 2019, *MNRAS*, 489, 401
- Zürcher, D. & More, S. 2019, *ApJ*, 874, 184